Université Pierre et Marie Curie

Habilitation à diriger des recherches

Spécialité: Physique des Particules

presentée par

Sandrine Laplace

Laboratoire de Physique Nucléaire et des Particules

Twelve years in ATLAS: selected topics

Soutenue publiquement le 14 décembre 2015, devant le jury composé de:

	Pierre Antilogus	LPNHE
Rapporteur	Lance Dixon	SLAC
Rapporteur	Kevin Einsweiler	LBNL
	Louis Fayard	LAL
Rapporteur	Luca Malgeri	CERN
Membre invité	Gregorio Bernardi	LPNHE

Contents

1 Curriculum Vitae

1.1 Personnel

- Born in August, 16th 1977 in Thonon-les-Bains, France. 1 child.

1.2 Education and positions

- July 2014-Oct. 2015: Scientific Associate at CERN; Meyrin, Switzerland. Co-convener of the $H \to \gamma\gamma$ subgroup; isolation harmonization and co-convener of the isolation forum.
- 2011 - currently: Researcher on ATLAS, LPNHE; Paris, France. Study of the spin of the Higgs boson in the diphoton channel; background studies in the same channel; improvements of the calorimetric isolation with pile-up; calorimeter crack calibration.
- 2003-2011: Researcher on ATLAS, LAPP; Annecy-le-Vieux, France. Work on backend readout of calorimeter; combined test beam of ATLAS; development of calorimeter software; preparation of Higgs boson search in the diphoton channel; study of cosmic muons during commissioning phase; study of π^0's with first collision data; measurement of diphoton differential cross-section.
- 2000-2003: PhD on BaBar LAL; Orsay, France. Measurement of branching ratios and time dependent CP analysis of $B \to \rho\pi$, $B \to 3\pi$ et $B \to a_0\pi$. Improvement of SVT radiation protection system. Work on CKMFitter. PhD supervisor: Andreas Hoecker.
- 1999-2000: DEA Champs, particules, matière; Orsay, France
- 1995-1999: Physics master at the University Joseph Fourier; Grenoble, France

1.3 Administrative and research responsibilities

- 2015-now: co-convenor of the Isolation Forum in ATLAS (around 20 active analyzers, and a larger number of "followers").
- 2014-2015: co-convenor of the Higgs to diphoton working group in ATLAS (around 60 analyzers)
- 2014: member of the organizing committee (chair of the session "run 1 legacy results") of the conference "Physics at LHC and beyond", Quy Nhon, August 2014.
- 2014: chair of the local organizing committee of the 8th FCC-ee workshop, LPNHE, Paris, Oct. 2014.
- 2013-2014: co-editor of the final run 1 publication on the spin study in the Higgs to diphoton channel.
- 2013-currently: co-convenor of the Higgs group of the french "Terascale" Research Group ("Groupement de Recherche" GDR, around 50 participants).
- 2012-2014: spokesperson for the Higgs ATLAS group in LPNHE (around 20 researchers).
- 2011-2014: member of the LPNHE laboratory council.
- 2011: co-editor of the publication on direct photon pairs differential cross-sections measurement (Phys.Rev. D85 (2012) 012003).

- 2010-2011: member of the organizing committee of the France-Asia particle physics school in 2011 (les Houches); discussion leader during the school.
- 2010-2011: member of the LAPP scientific council.
- 2010: co-editor of the publication "Readiness of the ATLAS Liquid Argon calorimeter for LHC collisions", Eur.Phys.J. C70 (2010) 723-753.
- 2008: organization of the open doors at LAPP-Annecy.
- 2008: member of organizing committee of the France-Asia particle physics school in les Houches.
- 2007-2009: member of the scientific council of Section 29 of the University of Savoie.
- 2006-2009: member of the french LHC communication group of IN2P3.
- 2005-2008: convener of the calorimeter reconstruction software in ATLAS (around 10 active programmers).
- 2005: Liquid Argon calorimeter run coordinator during the ATLAS combined testbeam.
- 2005-2013: responsible of the ATLAS-Vietnam group within the France-Vietnam International Associate Laboratory (LIA).
- 2004-2007: French representative of the CERN users committee (ACCU).
- 2003-2008: LAPP representative of the "Physique ATLAS France" (PAF) committee.
- 1999-2004: co-founder of CKMFitter.

1.4 Conferences, seminars, lectures

- 2014 (November 22): seminar "les grandes lecons d'un petit Boson" with Etienne Klein at the Palais de la Découverte, Paris.
- 2014 (November 9): seminar "le Boson de Higgs, prix Nobel 2013" in the Rencontres du Ciel et de l'Espace, Cité des Sciences et de l'Industrie, Paris.
- 2014 July 3rd: parallel talk "Higgs to two photons in ATLAS" in the 37th International Conference on High Energy Physics (Valencia, Spain).
- 2014 June 6th: seminar on the Higgs Boson discovery given at the "Nuit des Sciences" in ENS Paris
- 2014 February 7th: seminar on the Higgs Boson discovery given at the French Physics Society day ("Regards de Physicien(ne)s") in Paris.
- 2014 January 30th: seminar on the Higgs Boson discovery given at the Institut des Nanosciences de Paris (INSP) in Paris.
- 2012 December 4th: seminar on the Higgs Boson discovery given at the Laboratoire de Physique des Solides (LPS) in Orsay.
- 2012 August 13th: plenary talk "Higgs searches in ATLAS" at the conference SUSY 2012 (Beijing, China).

- 2012 July 13th: seminar on the Higgs Boson discovery given with M. Cacciari in the physics department of the University Paris 7.
- 2010 January: lecture on "statistics for particle physics" given at the 2nd LHC school in Vietnam (Ho Chi Minh, Vietnam).
- 2009 May 24th: plenary talk on "Commissioning of the ATLAS Liquid Argon Calorimeter" given at the the 11th Pisa Meeting on Advanced Detectors (Pisa, Italie).
- 2009 January: lecture on the Higgs boson at the 1st Vietnamese LHC school (Hanoi, Vietnam).
- 2006 July 3rd: plenary talk "Mass reconstruction method in SUSY" given at the conference Physics at LHC (Cracovie, Pologne).

1.5 Prizes

2012 December: Prix Thibaud from the Académie des Sciences, Belles Lettres et Arts de Lyon.

1.6 Students supervision

- 2014-now: at CERN, partial supervision (on typically 3 to 6 months small projects) of several students and post-docs within the groups I co-convened ($H \to \gamma\gamma$ and isolation forum) in ATLAS
- 2012-2013: supervision of two M2 students and two M1 students on ATLAS.
- 2008-2011: supervision of one PhD student in on ATLAS.

2 Introduction

2.1 Scientific context

The fundamental constituents of matter and their interactions (as "individual particles") are described by the Standard Model of particle physics. This model successfully describes all accelerator-based experimental results so far (excluding neutrino oscillations), but fails to describe the universe matter and energy content as a whole (in particular, the dark matter and energy). For this reason, and several other more "esthetical" reasons, it is now believed that "new physics" (like supersymmetry, extra dimensions, etc...) must complement the Standard Model.

One key piece of the Standard Model is the Higgs Boson, the excitation of the Higgs field that gives mass to particles by coupling to the particle fields. The "Higgs mechanism" [1–6] has introduced a huge change in the paradigm of what mass is for fundamental particles: not an intrinsic property of a particle, but an induced property created by the presence of a special field filling the vacuum. Even though this mechanism was invented in the 60's, its experimental proof, i.e. the existence of the Higgs Boson, eluded all searches until it was finally observed at the LHC.

The LHC (Large Hadron Collider) [7] was imagined in the 80's with the idea to explore the TeV scale to look for new physics, and undoubtedly find the Higgs Boson if it exists. The machine, and the four experiments built around it, took 30 years to design, build and commission. They all run very beautifully during the "LHC run 1" since 2009. "Surprisingly" (though this is a subjective statement), the Higgs Boson was discovered before any new physics: this is both because it finally took much less time than planned to discover the Higgs Boson, and because the new physics seems to be more elusive than what people were expecting.

The increase of energy of the LHC in run 2 (going from 8 to 13 TeV) yet opens a new door for the observation of new phenomena. This energy step is the last one foreseen in the field before at least 2 or 3 decades: no doubt that no stone will be left unturned in the coming years...

2.2 Personal contributions

After completing my PhD (2000-2003) on the BABAR experiment at SLAC, I joined the ATLAS experiment at the LHC, CERN. This report summarizes my work on ATLAS during the past 12 years, the driving line of which was the discovery and study of the Higgs Boson in its di-photon decay. I was lucky enough during this period to see most steps of this discovery: when I joined ATLAS in 2003, I participated in the combined testbeam to characterize a full slice of the ATLAS detector, with a personal focus on the Liquid Argon electromagnetic calorimeter. During the testbeam, I could therefore work on several aspects such as electronics (software of the Digital Signal Processor of the Readout Drivers of the calorimeter), data taking (shifts, weekly calorimeter run coordinator), electronics calibration (development of the corresponding software, analysis of the calibration data, database handling), reconstruction software (from calorimeter cells to clusters), and finally testbeam data analysis (study of converted photons). I then became coordinator of the calorimeter reconstruction software in ATLAS from 2005 to 2008, and started at the same period to work on prospective studies for the Higgs Boson search. When ATLAS recorded the first cosmic muons in the cavern in 2008, I analyzed these data to inter-align the calorimeter with the tracker, and to measure the calorimeter uniformity. With the first 900 GeV collisions in 2009, I repeated this latter measurement using photons from the $\pi^0 \to \gamma\gamma$ decay. With the first 7 TeV collisions in 2010 and 2011, I measured the direct photon pair production differential cross-sections, which constitutes the main background for the Higgs Boson search in the diphoton channel. In parallel, I developed a new isolation variable, much more robust against pile-up than the one existing so far, which is a key ingredient to reject the fake jet background in this search. After the Higgs Boson discovery, I studied the spin of the

newly discovered particle through the study of the angular distribution of the two outgoing photons. Finally, I became convener of the Higgs to two photons analysis group in 2014, in the period where most publications were produced by the group, which beautifully closed this 12 year period.

I will not describe in detail all these activities in this report, but I will focus on a few of them: the calorimeter uniformity, the isolation energy, the photon pair production cross-section, and the spin study.

3 LAr calorimeter uniformity with cosmic muons and first collisions

3.1 The ATLAS detector in a nutshell

The ATLAS detector is described in detail in Ref. [8]. ATLAS is a multi-purpose detector with a forward-backward symmetric cylindrical geometry. It uses a right-handed coordinate system with its origin at the nominal interaction point (IP) in the centre of the detector and the z-axis along the beam pipe. The x-axis points from the IP to the centre of the LHC ring, and the y-axis points upward. Cylindrical coordinates (r, ϕ) are used in the transverse plane, ϕ being the azimuthal angle around the beam pipe. The pseudorapidity is defined as $\eta = -\ln\tan(\theta/2)$, where θ is the polar angle.

At small radii from the beamline, the inner detector (ID), immersed in a 2 T magnetic field produced by a thin superconducting solenoid located in front of the calorimeter, is made up of fine-granularity pixel and microstrip detectors. These silicon-based detectors cover the range $|\eta| < 2.5$. A gas-filled straw-tube transition-radiation tracker (TRT) complements the silicon tracker at larger radii and also provides electron identification based on transition radiation. The electromagnetic (EM) calorimeter is a lead/liquid-argon sampling calorimeter with an accordion geometry. The EM calorimeter is divided into a barrel section covering $|\eta| < 1.475$ and two end-cap sections covering $1.375 < |\eta| < 3.2$. For $|\eta| < 2.5$ it is divided into three layers in depth, which are finely segmented in η and ϕ. An additional thin presampler layer, covering $|\eta| < 1.8$, is used to correct for fluctuations in energy losses of particles before they reach the calorimeter. Hadronic calorimetry in the region $|\eta| < 1.7$ uses steel absorbers and scintillator tiles as the active medium. Liquid argon with copper absorbers is used in the hadronic end-cap calorimeters, which cover the region $1.5 < |\eta| < 3.2$. A forward calorimeter using copper or tungsten absorbers with liquid argon completes the calorimeter coverage up to $|\eta| = 4.9$. The muon spectrometer (MS) measures the deflection of muon trajectories with $|\eta| < 2.7$, using three stations of precision drift tubes, with cathode strip chambers in the innermost layer for $|\eta| > 2.0$. The deflection is provided by a toroidal magnetic field with an integral of approximately 3 Tm and 6 Tm in the central and end-cap regions of the ATLAS detector, respectively. The muon spectrometer is also instrumented with dedicated trigger chambers, the resistive-plate chambers in the barrel and thin-gap chambers in the end-cap, covering $|\eta| < 2.4$.

3.2 The LAr calorimeter and its uniformity

The LAr calorimeter [9], shown in Figure 1, is composed of sampling detectors with full azimuthal symmetry, housed in one barrel and two endcap cryostats. More specifically, a highly granular electromagnetic (EM) calorimeter with accordion-shaped electrodes and lead absorbers in liquid argon covers the pseudorapidity range $|\eta| < 3.2$, and contains a barrel part (EMB [10], $|\eta| < 1.475$) and an endcap part (EMEC [11], $1.375 < |\eta| < 3.2$). For $|\eta| < 1.8$, a presampler (PS [11, 12]), consisting of an active LAr layer and installed directly in front of the EM calorimeters, provides a measurement of the energy lost upstream. Located behind the EMEC is a copper-liquid argon hadronic endcap calorimeter (HEC [13], $1.5 < |\eta| < 3.2$), and a copper/tungsten-liquid argon forward calorimeter (FCal [14]) covers the region closest to the beam at $3.1 < |\eta| < 4.9$. An hadronic Tile calorimeter ($|\eta| < 1.7$) surrounding the LAr cryostats completes the ATLAS calorimetry.

All the LAr detectors are segmented transversally and divided in three or four layers in depth, and correspond to a total of 182468 readout cells, i.e. 97.2% of the full ATLAS calorimeter readout.

The relative energy resolution of the LAr calorimeter is usually parameterized by:

$$\frac{\sigma_E}{E} = \frac{a}{\sqrt{E}} \oplus \frac{b}{E} \oplus c, \tag{1}$$

where (a) is the stochastic term, (b) the noise term and (c) the constant term. The target values for these terms are respectively $a \simeq 10\%$, $b \simeq 250$ MeV (without pile-up) and $c = 0.7\%$.

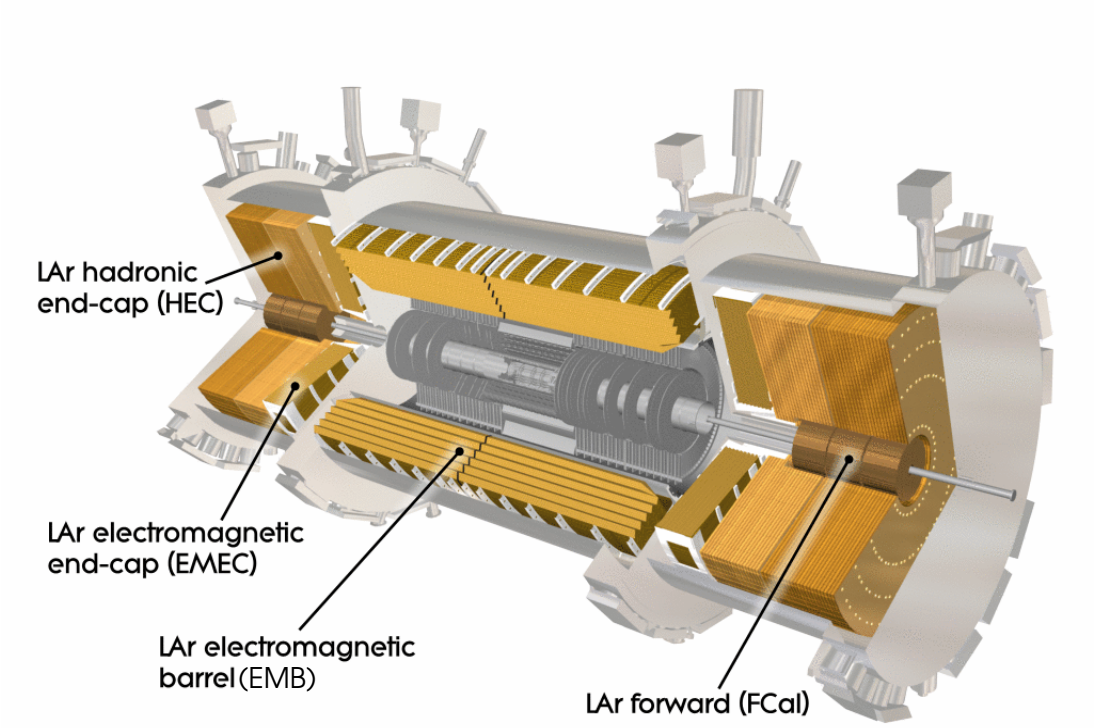

Figure 1: *Cut-away view of the LAr calorimeter.*

Any non-uniformity in the response of the calorimeter has a direct impact on the constant term in the energy resolution; great care was taken during the construction to limit all sources of non-uniformity to the minimum achievable, aiming for a global constant term below 0.7%.

The uniformity of the calorimeter was measured for three barrel production modules using electrons during beam test campaigns [15]. Before the availability of a large electron sample from collisions, the calorimeter uniformity could be checked in situ first using cosmic muons, and then using π^0ś from the first 900 GeV collisions.

The corresponding measurement can nevertheless not be directly extrapolated to high p_{T} electrons and photons. Indeed, in the case of cosmics, muons behave very differently from electrons: in most events, they deposit only a minimum ionization energy in the liquid argon and they are much less sensitive to upstream material. Also, the cosmic run statistics are limited, so uniformity cannot be studied with cell-level granularity, and only in the barrel calorimeter (due to both the topology of the cosmic muon events and the choice of triggers). In the case of π^0's, the uniformity is measured for low-energy photons only that are reconstructed and calibrated with different algorithms than those used for higher energy electrons and photons .

The goal of the cosmic muon and π^0 analyses is rather to quantify the agreement between data and Monte Carlo, and to exclude the presence of any significant non-uniformity in the calorimeter response.

3.3 The basics of energy reconstruction

When an electron or photon reaches the electromagnetic calorimeter, it interacts with the lead absorbers to create secondary particles, which will further create tertiary particles, and so on, yielding an electromagnetic shower. The daughter charged particles of the shower then ionize the liquid Argon.

Because of their higher mass, most often [1] the muons rarely interact with the lead absorbers and directly ionize the liquid Argon without creating an electromagnetic shower (which justifies their name of "Minimum Interacting Particles", MIP). They therefore deposit very little energy in the electromagnetic calorimeter.

In both cases, the ionization electrons drift towards the readout electrode thanks to the high voltage applied between the absorbers and the electrodes. The signal collected on the electrodes has a triangular shape with a typical duration of 400 ns (which is 8 or 16 times longer than the collision frequency of 50 ns in run 1, and 25 ns in run 2), as shown in Fig. 2. The amplitude of the triangular signal is directly proportional to the energy deposited by the incoming particle in a given calorimeter cell.

The triangular signal is then transformed by the readout electronics: it is pre-amplified, shaped with a bipolar filter, sampled every 25 ns, and converted into an analogic signal. The bipolar shape, shown on Fig. 2, yields a null total integral and allows to minimize the impact of the pile-up of signals due to the long integration time compared to the LHC bunch crossing.

Typically, 4 or 5 samples of the bipolar shape (around the peak) are sufficient to properly reconstruct the amplitude and time of the initial triangular signal. To minimize the impact of the electronics and pile-up noise, the samples are weighted with Optimal Filter Coefficients (OFC). Finally, the reconstructed amplitude (in ADC counts) is converted into energy (in MeV) with a set of conversion factors.

The incoming particles usually deposit their energy in several contiguous cells. One should thus reconstruct clusters of cells to collect most of the deposited energy. For the objects considered here (electrons, photons, muons), the clusters consist of rectangles of cells collected across the layers of the electromagnetic calorimeter. The clusters are then calibrated to account for the energy not collected

[1] The muons sometimes encounter "catastrophic energy losses" creating an electromagnetic shower.

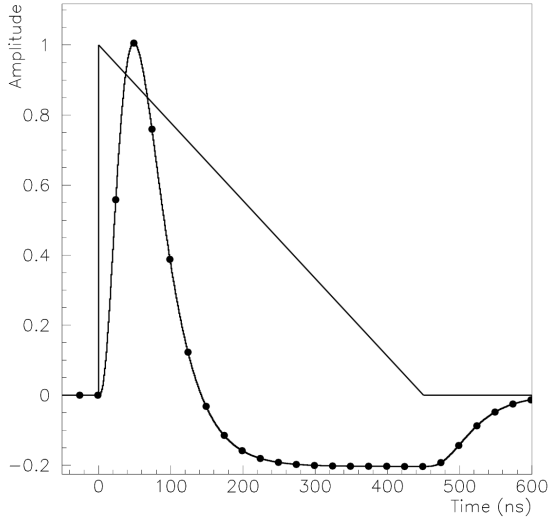

Figure 2: *Ionisation current as a function of time before (triangular shape) and after (bipolar shape) the electronic shaping.*

by the cluster (losses before the calorimeter, or in dead material of the calorimeter, or outside the cluster).

For the uniformity studies using cosmic muons, a dedicated rectangle cluster was used and no calibration needs to be applied since muons behave like MIP in the calorimeter. For the π^0ś of the first LHC collisions, another type of clustering algorithm, called topological clustering, was used in order to reach smaller energies: it consists of aggregating contiguous cells based on energy over noise ratios. The resulting cluster is not rectangular. A special calibration was then applied to recover the proper π^0 energy.

3.4 Uniformity using cosmic muons

This analysis [16] uses the 2008 cosmic data for which both the muon spectrometer and inner detector were operating and were used for triggering and event selection. The data sample consists of filtered events requiring a reconstructed track in the inner detector with at least one hit in the silicon tracker and reasonably projective. To reconstruct the full muon track in the inner detector, a dedicated algorithm looks for a single track crossing both the top and bottom hemispheres. This single track is then extrapolated both downward and upward into the calorimeter. Since the cosmic muons reach the calorimeter at random times, a special iterative procedure [2] is applied to apply the right set of OFC (see Sec. 3.3).

In order to perform the most accurate evaluation of the calorimeter uniformity, the measurement

[2]Since most muons are minimum ionizing particles, the muon signal is small, typically 150 MeV is deposited in the most energetic cell in the second layer, only five times the noise, and many cells do not pass this threshold. Therefore, an alternative reconstruction is used in this analysis: in the first pass, the iteration threshold is lowered to zero so that the timing is computed for most of the cells. In the second pass, the timing of the most energetic cell determined in the first pass is applied to all the other cells of the road.

granularity, the cluster size and the selection cuts have been optimized.

The binning is determined by requiring a minimum of 500 events per unit. In the η direction, this corresponds to bins of 0.025 (equal to the second layer cell width) up to $|\eta| = 0.7$ and wider bins above.

In the first layer, the muon energy loss is measured using a $\Delta\eta \times \Delta\phi = 2 \times 1$ (in units of first layer cells) cluster, which contains most of the deposited energy. Adding an additional cell brings more noise than signal. In the second layer, a 1×3 (in second layer cell unit) cluster is used: it suffers less from noise than a 3×3 cluster, but requires the removal of non-projective events which leak outside the cluster along the η direction. This projectivity cut is based on the centrality of the muon in the second layer cell: when the muon passes close to the edge of the cell, a very small non-projectivity induces a large energy leakage into the neighboring cell. Therefore, for each second layer cell, eight bins corresponding to the eight first layer cells located in front of it were defined, and in each bin a cut is applied on the beam impact parameter z_0 of the track, such that the muon is geometrically contained in the second layer cell.

The remaining statistics after this projectivity cut is 76 k events in the data sample and 113 k events in the Monte Carlo sample. The events are mainly located under the cavern shafts leading to a coverage of around 20% of the full electromagnetic barrel calorimeter.

A comparison of the energy reconstructed in the first and second layers between data and Monte Carlo events is shown in Figure 3. The width of these distributions is larger in the case where all events are used (left) compared to a single η-bin (right), because the energy deposit is η-dependent.

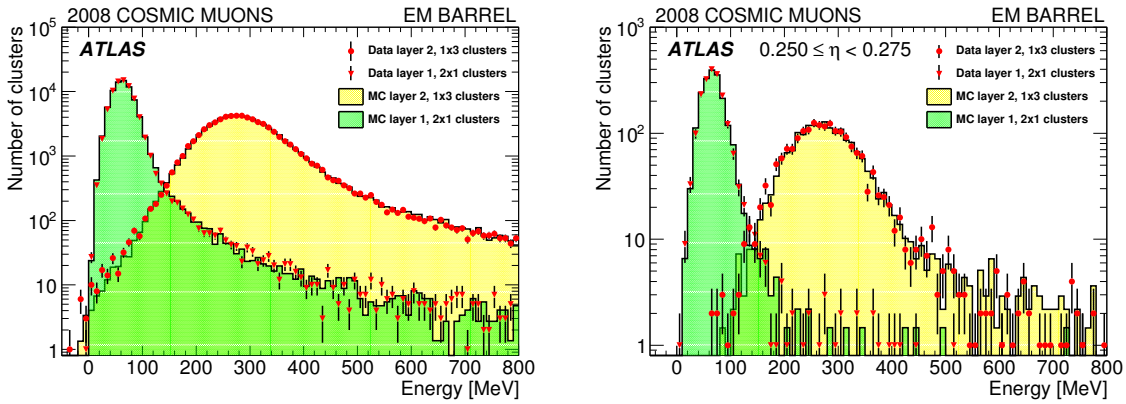

Figure 3: *Energy in a* 2×1 *cluster in the first layer (histogram for Monte Carlo and triangles for data) and in a* 1×3 *cluster in the second layer (histogram for Monte Carlo and full circles for data) for all events (left) and a single* η*-bin (right).*

The agreement between the data and Monte Carlo distributions is very good, both for the shape and for the absolute energy scale which differs by only 2% in the front layer and 1% in the second layer. Part of the difference comes from the slight difference in acceptance for data and Monte Carlo, as well as from the difference in energy reconstruction. This overall energy scale difference is corrected for in the MC in the rest of the study.

Given the limited statistics of the projective cosmic muon data, the uniformity of the response in η cannot be estimated at the cell level. A natural choice of cell combination is to integrate clusters in ϕ since the response should not vary along this direction due to the ϕ symmetry of the calorimeter. The response along the η direction for cosmic muons depends on the variation of the amount of liquid argon seen by the muon. In particular, a transition occurs at $|\eta| = 0.8$ where the lead thickness goes

from 1.53 mm to 1.13 mm.

The estimation of the muon energy in each η-bin is done with a fit of the cluster energy distribution using a Landau function convoluted with a Gaussian. The Landau function accounts for fluctuations of the energy deposition in the ionization process and the Gaussian accounts for the electronic noise and possible remaining fluctuations. In particular, a 10% difference is observed between the width of the Gaussian expected from the electronic noise and the width of the fitted Gaussian. This bias mostly comes from remaining cluster non-containment effects which are found to be η-independent and thus do not produce any artificial non-uniformity. The most probable value (MPV) of the Landau distribution estimates the energy deposition.

Distributions of data and Monte Carlo MPVs along the η direction for the first and second layers are shown in Figure 4.

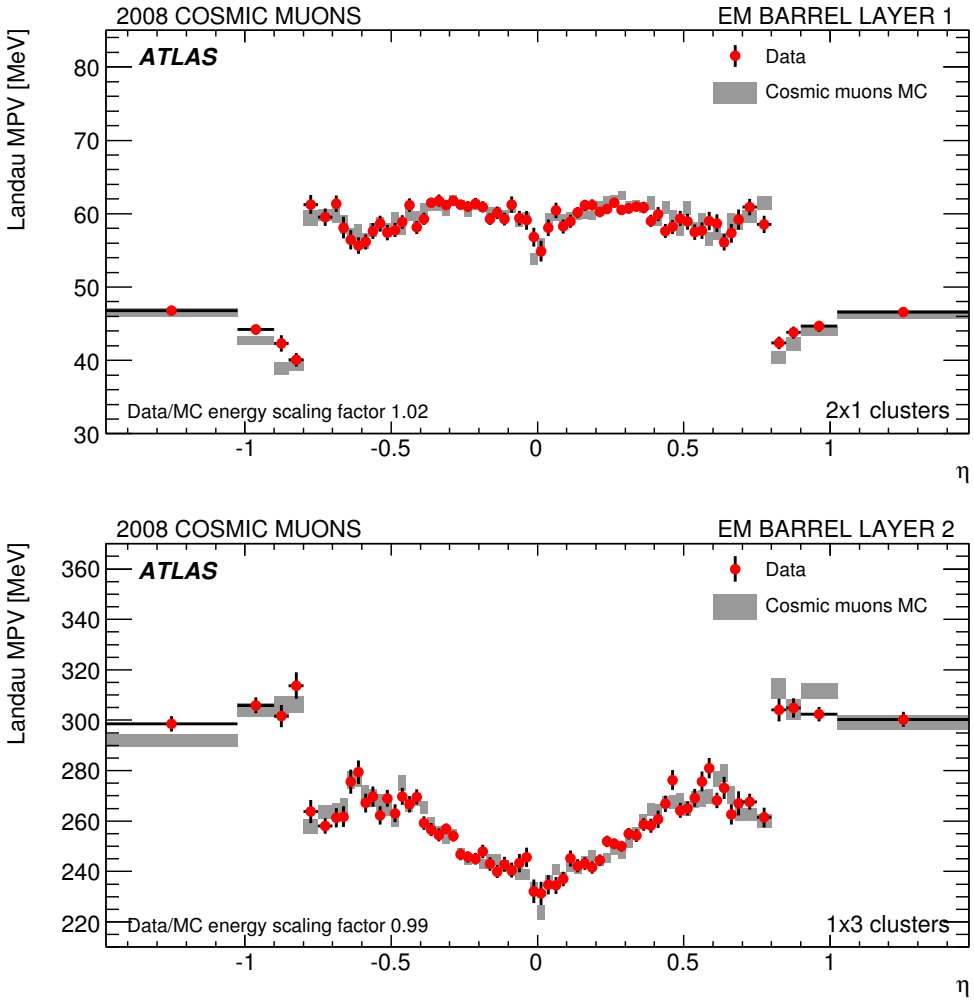

Figure 4: *Landau MPV as a function of η in the first (top) and second (bottom) layers for the data (red points) and Monte Carlo (grey bands).*

In the first layer, the MPVs are roughly constant along η, except around $\eta = 0$ where some cells are physically missing in the detector, and around $|\eta| = 0.6$ where the cell depth is varying. In the second layer, the response follows a typical "V-shape" corresponding to the variation of the cell depth along η that rises up to $|\eta| = 0.6$. Again, the agreement between the data and Monte Carlo is very

good, showing that the contribution of systematic effects due to the energy reconstruction method or the non-projectivity of the tracks is small.

The response uniformity $U_{\rm meas}$ is given by the RMS of the normalized differences between the data and Monte Carlo MPVs in each η-bin :

$$U_{\rm meas} = \sqrt{\frac{\sum_{i=1}^{N_{\rm b}} (U_{i,\rm meas} - < U_{i,\rm meas} >)^2}{N_{\rm b}}}, \tag{2}$$

with:

$$U_{i,\rm meas} = \frac{MPV_{i,\rm Data} - MPV_{i,\rm MC}}{MPV_{i,\rm Data}} \ , \tag{3}$$

where $U_{i,\rm meas}$ is averaged over ϕ, $N_{\rm b}$ is the number of bins in η, and $<U_{i,\rm meas}>=0$ since the global energy scale difference was corrected by rescaling the MC.

The measured uniformity should be compared to the expected uniformity $U_{\rm exp}$, which is obtained similarly to Eq. 2 with $U_{\rm i,exp}$ given by:

$$U_{i,\rm exp} = \frac{MPV_{i,\rm MC}}{MPV_{i,\rm Data}} \sqrt{U_{i,\rm Data}^2 + U_{i,\rm MC}^2} \tag{4}$$

with:

$$U_{i,\rm Data(MC)} = \frac{\sigma(MPV_{i,\rm Data(MC)})}{MPV_{i,\rm Data(MC)}}, \tag{5}$$

where $\sigma(MPV_{i,\rm Data(MC)})$ is the statistical uncertainty on the measured Landau MPV. This uncertainty is due to the finite statistics of the data and Monte Carlo samples in each bin, the Landau dispersion of the ionization, and the electronic noise.

The measured uniformity $U_{\rm meas}$ should agree with the expected uniformity $U_{\rm exp}$ if the Monte Carlo simulation reproduces the data well: the key ingredients are the acceptance, the muon spectrum, and the energy reconstruction method. A significant departure of the measured uniformity from the expected one would be a measurement of additional non-uniformities U_Δ ($U_\Delta^2 = U_{\rm meas}^2 - U_{\rm exp}^2$).

The measured and expected uniformities for the two EM layers are shown in Figure 5.

The fluctuations of the measured energies are large: the RMS of the corresponding distribution is $2.4 \pm 0.2\%$ in the first layer and $1.7 \pm 0.1\%$ in the second layer, showing that the statistical power of the analysis is limited given the available data and Monte Carlo statistics. The fluctuations mostly remain within the limits of the band representing the expected values. The RMS of the latter distribution is 2.2 % in the first layer and 1.6 % in the second layer. This demonstrates that no significant additional non-uniformity (U_Δ) is present in the data. An upper limit is derived and yields $U_\Delta < 1.7\%$ @ 95% CL in the first layer, and $U_\Delta < 1.1\%$ @ 95% CL in the second layer.

The calorimeter response uniformity along η (averaged over ϕ) measured with the 2008 cosmic muons is thus consistent at the percent level with the Monte Carlo simulation and shows no significant non-uniformity.

3.5 Uniformity using π^0's from first collisions

This second analysis [17] (which constitutes one of the PhD topic of my student M. Aurousseau [18]) is based on a data sample collected at $\sqrt{s} = 900$ GeV from early 2010. The data sample consists of 493683 collision candidates which corresponds to an integrated luminosity of approximately 11.5 μb^{-1}. The Monte Carlo event sample consists of non-diffractive minimum-bias events generated with the ATLAS Pythia tune and passed through the full ATLAS simulation and reconstruction software.

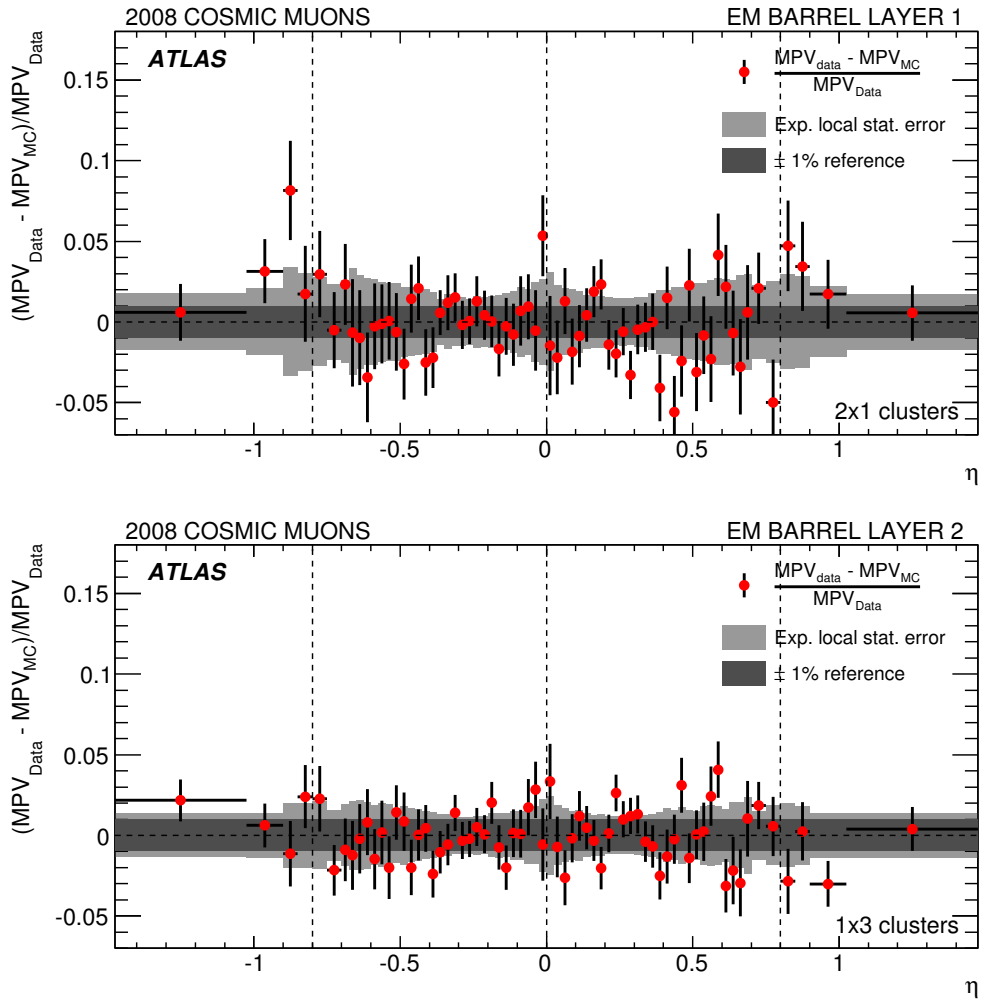

Figure 5: *Measured $U_{i,\mathrm{meas}}$ (red points) and expected $U_{i,\mathrm{exp}}$ (light grey band) cosmic muon energy dispersions as function of η for the first (top) and second (bottom) layers of the EM barrel. The dark grey band indicates a $\pm 1\%$ strip for reference.*

For low-energy photons, the standard sliding window clustering developed for high-E_{T} objects with a seed threshold set to $E_{\mathrm{T}} = 2.5$ GeV is inefficient. Instead, low-energy photons are flagged using EM topological clusters. These clusters are reconstructed with a seed cell threshold $|E_{cell}| = 4\sigma$ (where σ is the expected RMS of electronic noise in the cell) and are requested to have a transverse energy $E_{\mathrm{T}} > 300$ MeV. Rectangular clusters of size $\Delta\eta \times \Delta\phi = 0.075 \times 0.125$, which corresponds to an area of 3×5 cells in the middle layer of the EM calorimeter, are then built on top of the topological clusters.

The energy in the three layers of the calorimeter is defined at the electromagnetic scale. The energy of the presampler cells has a factor 20 (60 in the end-cap) applied to the deposited energy in the liquid argon layer, which is the typical factor required for first-order upstream energy-loss correction for high-energy electrons and photons.

To account for upstream energy-loss and lateral and longitudinal leakages, the rectangular clusters are calibrated using the longitudinal weights method (LW), which has been tested with data in an ATLAS combined test-beam for electrons [19] with energy > 10 GeV. In the LW method, the reconstructed cluster energy (E_{rec}) is calculated as a linearly weighted sum of the layer responses:

$$E_{rec} = s(b + W_0 E_{PS} + E_1 + E_2 + W_3 E_3) \tag{6}$$

where E_{PS} and $E_{i=1,2,3}$ are the cluster energies in the presampler and the three layers of the calorimeter. The coefficients s, b,W_0, and W_3 are called longitudinal weights and depend only on the pseudo-rapidity position of the cluster. Their purpose is to provide optimum linearity and resolution. They are calculated by a χ^2 minimization of $(E_{true} - E_{rec})^2/\sigma_E^2$ using Monte Carlo, where σ_E is the calorimeter energy resolution and E_{true} is the true photon MC energy. The coefficients extracted for higher energy objects cannot be used in this low-energy regime, as the method does not have any energy dependence. A dedicated set of coefficients has been extracted using low-energy photons coming only from π^0's in the minimum-bias simulation sample with a binning of 0.025 along $|\eta|$ (assuming ϕ symmetry). In order to remove the effect of non-Gaussian tails, only photons in the core of the distribution are used in each η bin.

In order to extract the π^0 signal from the combinatorial background, the following criteria are applied:

- a cluster-removal procedure is applied to avoid energy-sharing between two clusters: if two clusters overlap, they are both rejected.

- the distributions of the fraction of energy in the first layer $E_1/(E_1+E_2+E_3)$ for signal (photons candidates from π^0 decays) and background (which arises dominantly from charged hadrons) using simulation are compared in Fig. 6. Since the low-energy photons deposit a significant amount of their energy in the first layer of the electromagnetic calorimeter, this fraction is required to be larger than 0.1.

- the cluster transverse energy should be greater then 400 MeV, and the acceptance is limited to $|\eta| < 2.37$, excluding clusters reconstructed in the transition region between the barrel and end-cap cryostats, $1.37 < |\eta| < 1.52$.

Among all possible pairs of photons, only the combinations with $p_{\mathrm{T}}^{pair} > 900$ MeV are retained. A total of about 8×10^5 photon pairs are selected in the data.

The invariant mass distribution of the photon pairs is shown in Fig. 7 for both data and Monte Carlo. A clear excess of events can be observed near the π^0 mass. The diphoton mass distribution is fitted using the following procedure: the signal is described by the sum of a Gaussian and a Crystal-Ball function, which are required to have the same mean. The combinatorial background is described with a 4th order Chebyshev polynomial. The parameters of the signal and the background normalization

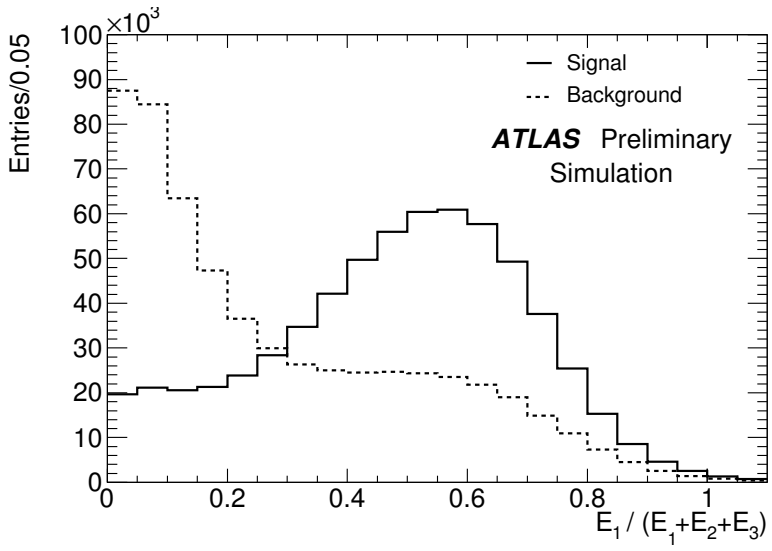

Figure 6: *Distribution of the fraction of energy in the first layer $E_1/(E_1 + E_2 + E_3)$ for signal (solid line) and background (dashed line).*

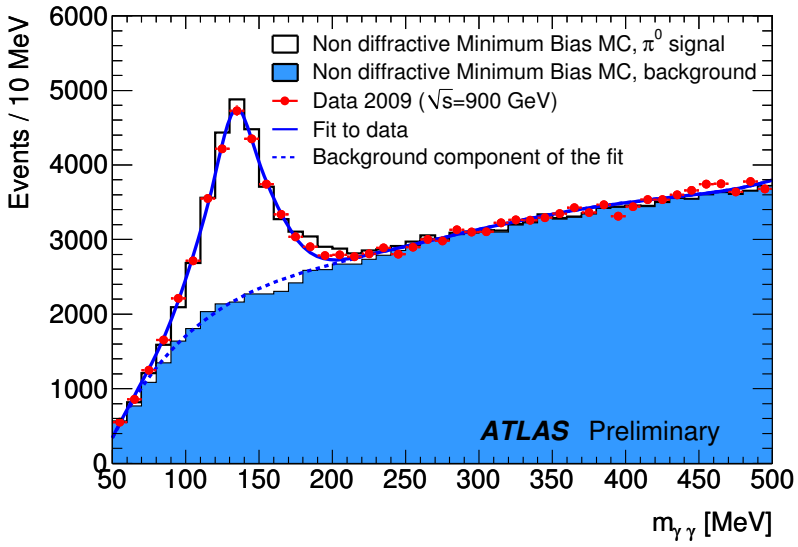

Figure 7: *Diphoton invariant mass after application of the selection criteria for data and Monte Carlo. The Monte Carlo is normalized to the same number of entries as the data.*

are free parameters for the fit applied to the data, while the parameters of the Chebyshev polynomial have been extracted from the Monte Carlo.

The measured π^0 mass is $134.0 \pm 0.8(stat)$ MeV for the data and $132.9 \pm 0.2(stat)$ MeV for the Monte Carlo. The resolution [3] of the signal distribution is 24.0 MeV, to be compared with 25.2 MeV in the simulation, and the number of π^0's extracted from the fit is $(1.34 \pm 0.02(stat)) \times 10^4$.

This fit is sensitive to the modeling of the background shape near the π^0 mass. The signal resolution and the number of signal events are especially sensitive to this modeling. Varying the background shape under the peak leads to a difference of up to 1% for the fitted π^0 mass, up to 10% for the fitted π^0 mass resolution and up to 20% for the fitted total number of signal events. The 1% agreement of energy scale between data and Monte Carlo is well within the $2-3\%$ expected uncertainty on the energy scale, transported from the test-beam measurement and limited by the knowledge of the liquid argon temperature in the test-beam setup. The 1.5% discrepancy of the Monte Carlo mass with respect to the PDG nominal π^0 mass is consistent with the expected accuracy of the specific cluster calibration procedure for low-energy photons and the 1% uncertainty on the fitted π^0 mass arising from the background modeling.

In order to study the uniformity of the EM calorimeter response, the data are divided into ten η bins, and both photons from each π^0 candidate must fall in the same bin. The diphoton mass distribution in each η bin is fitted separately, while the background shape is fixed from the Monte Carlo for each η bin. The systematic uncertainty on the extracted mean of the π^0 mass peak is estimated by varying the background and signal shapes in the fit.

The result for the π^0 mass uniformity as a function of η are shown in Fig. 8. The reconstructed π^0 mass is constant within 3% for both data andMonte Carlo; the agreement between data and Monte Carlo (which tests the uniformity of the EM calorimeter response with respect to pseudo-rapidity) is at the level of $\pm 2\%$(limited by statistical uncertainties). This analysis extends the one performed with cosmic muons, which was not sensitive to material effects, where the uniformity in pseudo-rapidity bins of size 0.025 was checked to be within $\pm 1\%$ in the central region of the EM calorimeter.

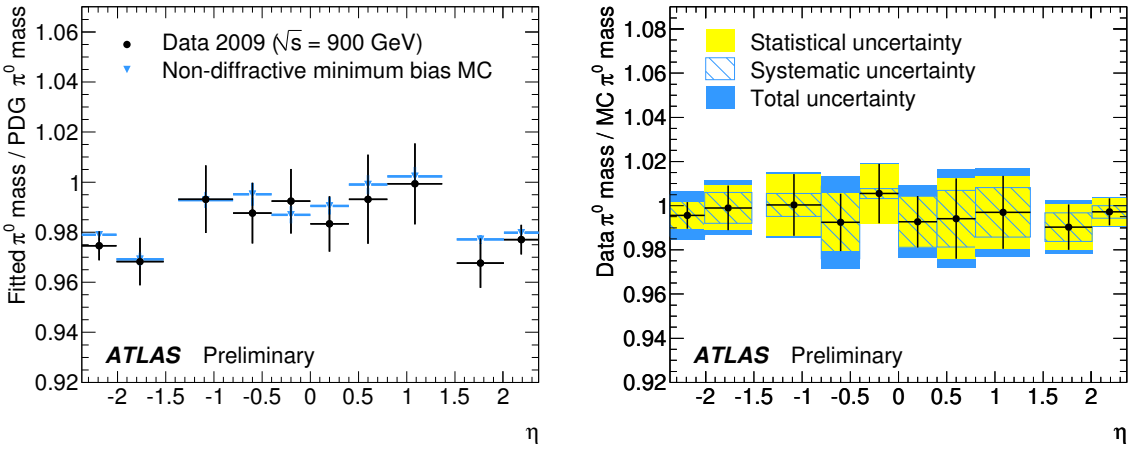

Figure 8: *Uniformity vs η of the π^0 mass fit result. The data are shown normalized to the PDG value of the π^0 mass (a) and the Monte Carlo fit result (b). Only statistical uncertainties are considered for the left-hand plot.*

Furthermore, the diphoton invariant mass when both photons are reconstructed in the EM barrel

[3] The resolution is defined such that the integral of the signal function from $< m > -\sigma$ to $< m > +\sigma$ is equal to 68% of the total signal integral (where $< m >$ is the π^0 mass extracted from the fit).

	Data	MC
All	$134.0 \pm 0.8(stat)$	$132.9 \pm 0.2(stat)$
Barrel	$136.6 \pm 0.6(stat)$	$136.7 \pm 0.1(stat)$
End-cap	$131.8 \pm 0.4(stat)$	$132.2 \pm 0.2(stat)$

Table 1: *Diphoton invariant mass fit results when (All) all the diphoton candidates are considered, (Barrel) both photons are required to be reconstructed in the EM barrel, (End-cap) both photons are required to be reconstructed in the EM end-cap.*

(endcap) is shown in Fig. 9. The distributions are fitted using the function described in Section 5.2. The results of the fits, shown in Fig. 5 and Fig. 7, are summarized in Table 1. The resolution is better in the end-cap region where higher energy photons are reconstructed.

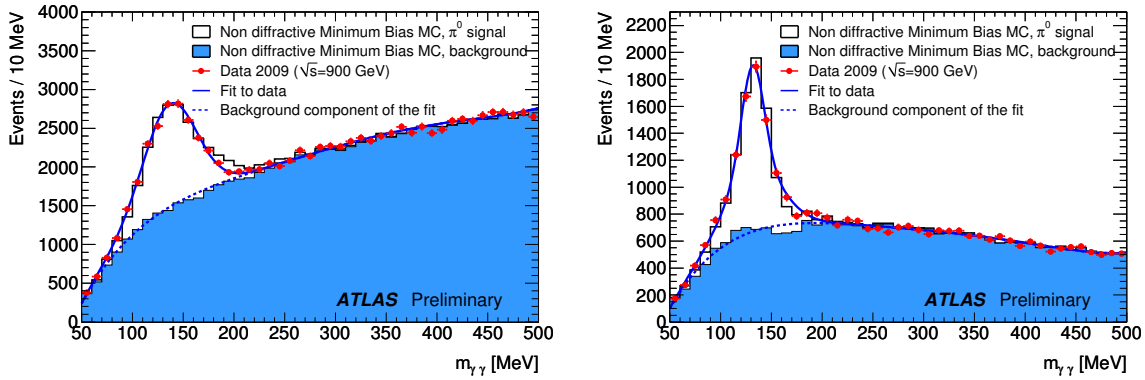

Figure 9: *Diphoton invariant mass fit when (a) both photons are required to be reconstructed in the EM barrel, (b) both photons are required to be reconstructed in the EM end-cap.*

3.6 Uniformity at the end of run 1, and conclusions

The uniformity measurement obviously got more precise using $Z \to e^+e^-$ events from the run 1 dataset (I did not participated in this study).

Figure 10 shows the azimuthal non-uniformity before and after some corrections described in [20]. The energy response is probed using the electron pair invariant mass peak in $Z \to ee$ events, and the non-uniformity is defined from the RMS of the response versus ϕ, probed with a granularity of $\Delta\phi = 0.025$, corresponding to one cell in the middle layer, and for coarse η bins; the contribution of the expected statistical fluctuations is subtracted in quadrature. The result can be interpreted as the non-uniformity contribution to the long-range resolution constant term. A non-uniformity of 0.45% is achieved for $|\eta| < 0.8$, and 0.75% is obtained in the rest of the calorimeter.

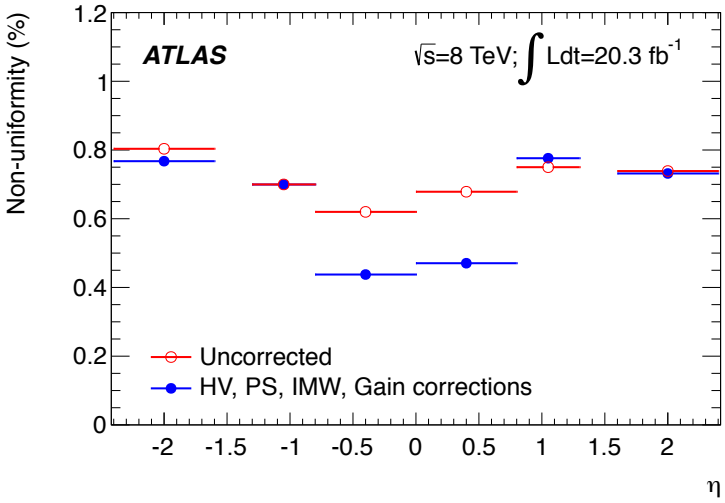

Figure 10: *Azimuthal non-uniformity of the energy response as a function of η, estimated from the electron pair invariant mass peak in $Z \to ee$ events.*

4 The isolation energy

4.1 Introduction

Most of the interesting physics signatures at the LHC require the identification of prompt non-fake leptons (electrons and muons) and photons. For example, the $H \to \gamma\gamma$ search requires to reduce drastically the amount of background coming from jets.

Prompt particles are those not coming from a hadron or tau decay. Non-fake particles are those which type was properly reconstructed (*i.e.* a non-fake reconstructed electron is a true electron, not another mis-identified particle). Non-prompt or fake electrons can arise from semi-leptonic decays of b and c quarks, photon conversions and jets with large electromagnetic energy (from the hadronisation to π^0's or coming from early showering in the calorimeter). Non-prompt or fake muons can originate from semi-leptonic decays of b and c quarks, from charged hadron decays decays in the tracking volume or in hadronic showers, or from punch-through particles emerging from high-energy hadronic showers. Non-prompt or fake photons come from hadron decay (mostly π^0's) or mis-identified electrons.

The prompt and non-fake leptons/photons are usually isolated, without much activity around them. It is therefore important to define a proper "isolation energy" around leptons and photons to reduce the contamination from non-prompt and fake objects.

Photons are nevertheless special objects compared to leptons, because prompt and non-fake photons can also originate from quark fragmentation. The collinear limit of this process becomes non-perturbative, and usually, one applies some kind of isolation already has to be applied in the theory computation.

The isolation energy relies on the tracker (which provides a more pile-up independent isolation) and on the calorimeter (which detects also neutral hadrons). These detectors are usually used to compute two separate isolations, and analyses use one or both these variables (in most analyses, using both is more powerful, except in a very boosted regime where the calo isolation is not appropriate because of the finite cells size). The particle flow algorithm, which was not available in run 1 but will be for run 2, combines the tracker and calorimeter information to take the best of each detector.

4.2 Calorimetric Isolation

The historical computation of calorimetric isolation was simply summing the transverse energy of the calorimeter cells (from both the electromagnetic and hadronic calorimeters) within a cone centered around the lepton/photon direction. This **etcone** variable showed bad performances in the beginning of run 1 for what concerns the pile-up resilience and data-Monte Carlo agreement. A significant improvement was brought by collecting the transverse energy of topological clusters instead of cells, thus effectively applying some noise-suppression algorithm to the cells.

Topological clusters [21] are clusters seeded by cells with an energy more than four times above the noise threshold of that cell. The clusters are then expanded by adding neighboring cells (in the three spatial directions, across all calorimeter layers, excluding the cells from the Tile gap scintillators) that have an energy more than two times above the noise level. After the expansion around the cluster stops, a last layer of cells is added around the cluster. The topological clusters used in the isolation computation are not further calibrated: they remain at the electromagnetic scale.

The electron and photon directions are given by the position of the associated rectangular calorimeter cluster used to reconstruct the electron/photon energy. The muon direction is given by the weighted mean of the extrapolated positions of the muon track into the electromagnetic calorimeter. All positive energy topological clusters which barycenter falls within a cone centered around the lepton/photon direction are summed into what is called the raw **topoetcone** isolation $E_{\mathrm{T,raw}}^{\mathrm{isol}}$. This is illustrated on Fig. 11.

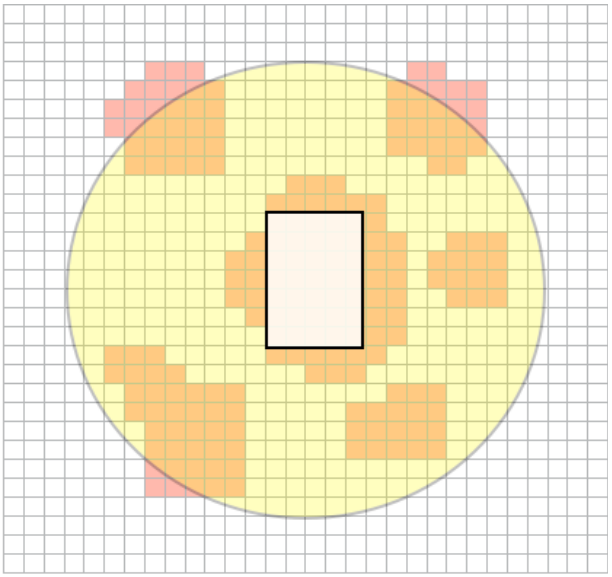

Figure 11: Schema of the **topoetcone** variable: the grid represents the middle calorimeter cells in the η (horizontal) and ϕ (vertical) directions. The lepton/photon is located in the center of the yellow cone representing the isolation cone. All topological clusters, represented in red, whose barycenter falls into the isolation cone are included in the isolation computation. The 5×7 cells white rectangle corresponds to the subtracted cells in the default "core subtraction" method.

The isolation energy described above still includes the lepton/photon energy, called the core energy $E_{\mathrm{T,core}}$, that needs to be subtracted. Several methods can be used to do so, depending on the object:

- **coreMuon**: this method is used to subtract the muon energy, by summing the cells in fixed windows (which size is optimized to collect the muon energy) in each of the calorimeter layer.

- **core57cells**: this is the run 1 way of subtracting the electron or photon core energy, simply by removing the cells included in a 5×7 rectangle around the electron/photon direction. The advantage of this simple method is to have a stable subtraction for real or fake objects for any transverse momentum and pile-up. The dis-advantage is that this does not subtract all the electron/photon energy and an additional leakage correction is needed. This is the default core subtraction technique for electrons and photons.

- **coreCone**: what seems to be the most obvious way to subtract the electron/photon energy from the isolation is to remove the topological clusters (there can be several) associated with the lepton/photon. In this case, most of the lepton/photon energy that contributes to the isolation is removed event by event and for electrons/photons, a smaller leakage correction is needed (typically 10 GeV at 3 TeV instead of 70 GeV with **core57cells**). Nevertheless, it is not straightforward to properly select the topological clusters associated to the lepton/photon, due to the presence of pile-up clusters, and in the case of fake leptons/photons. This will be studied in more details in run 2.

When the electron/photon core energy is subtracted from the isolation energy using the **core57cells** technique described above, some remaining electron/photon energy is leaking into the isolation cone and should be further subtracted. This leakage is evaluated using Monte Carlo samples of single electrons and photons without pile-up, which p_{T} spectrum goes up to 3 TeV. The samples are split into 10 η bins (where η corresponds to the barycenter of the energy deposited in the middle sampling of the electromagnetic calorimeter), and separate corrections are derived for calibrated [20] electrons, converted photons and unconverted photons. An example of the isolation energy distribution in a given η bin is shown as a function of p_{T} on the right side of Fig. 12, and a one dimensional slice in a given p_{T} bin is shown on the left side. The estimator used to quantify the leakage energy is the most-probable value (μ_{CB}) of a Crystal-Ball function (consisting of a Gaussian core portion and a power-low tail above a given threshold). This value is obtained through a global fit versus p_{T} in each η bin (indicated as a black line on the right side of Fig. 12,), and is then used to correct the isolation energy:

$$E_{\mathrm{T,leakage}}(p_{\mathrm{T}}) = \mu_{\mathrm{CB}}(p_{\mathrm{T}}) \times E_{\mathrm{cal}}/\cosh(\eta_{\mathrm{cluster}}), \tag{7}$$

where E_{cal} is the calibrated energy of the electron/photon and η_{cluster} is the associated cluster η position (corresponding to the barycenter of the η positions in the different layer of the electromagnetic calorimeter).

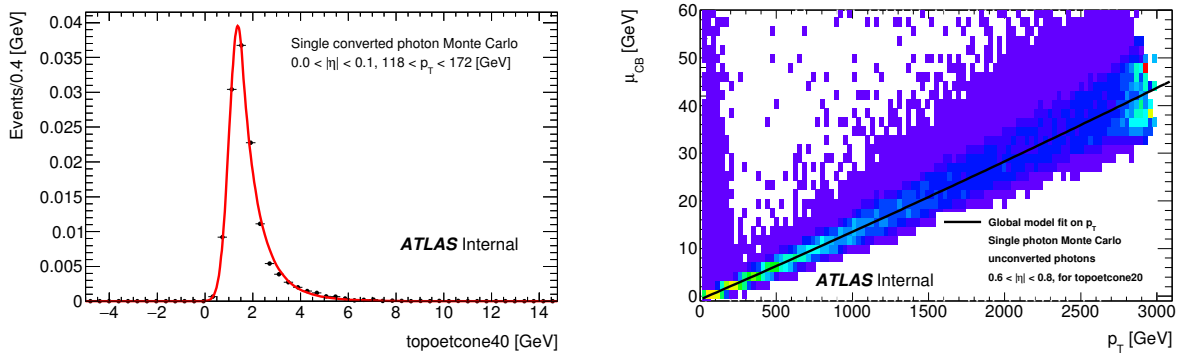

Figure 12: Left: fit of topoetcone20 (*i.e.* topoetcone with a cone size of 0.2) in a given η and p_{T} bin for converted photons with a Crystal-Ball function . Right: μ_{CB} as a function of p_{T} for unconverted photons, overlaid to the isolation distribution used to perform the global fit.

There are two important limitations to this leakage estimation:

- it is evaluated *on average*, *i.e.* it does not account from the shower shape fluctuations at a given p_{T}, which can get very large at high p_{T}.
- it is evaluated from the Monte Carlo, whereas the ATLAS Monte Carlo is known to not well reproduce the lateral shower shapes for electrons and photons.

The **coreCone** technique described earlier is a promising way to solve both of these issues, and will be carefully studied in run 2.

The pile-up and underlying event contribution to the isolation cone is estimated event by event using the technique of the ambient energy density. The ambient energy of a given event is computed in the following way using the **FastJet** [22] package:

- one reconstructs from positive energy topological clusters in the whole calorimeter acceptance (up to $\eta = 5$) jets with an anti-kT algorithm of size 0.5, with no p_{T} threshold.
- the area A_{i} of each jet in the event is estimated from a Voronoi tessellation algorithm.
- the energy density of each jet is computed as $\rho_i = p_{\mathrm{T,i}}/A_{\mathrm{i}}$.
- the median of the distribution of all the energy densities in the even, ρ_{median}, is used as an estimator of the energy density of the event.

Figure 13 (left) shows the distribution of ρ_{median} as a function of η in 13 TeV $Z \to e^+e^-$ Monte Carlo events. For this figure, ρ_{median} is estimated from jets contained in a sliding window located between η and $\eta + 3$. The quantity ρ_{median} is flat in the central η region, and decreases in the forward η region. For simplicity, ρ_{median} is finally estimated on average in each of these regions: a central region with $|\eta| < 1.5$ and a forward region $1.5 < |\eta| < 3$. The right plot of 13 shows the distribution of ρ_{median} in these two regions.

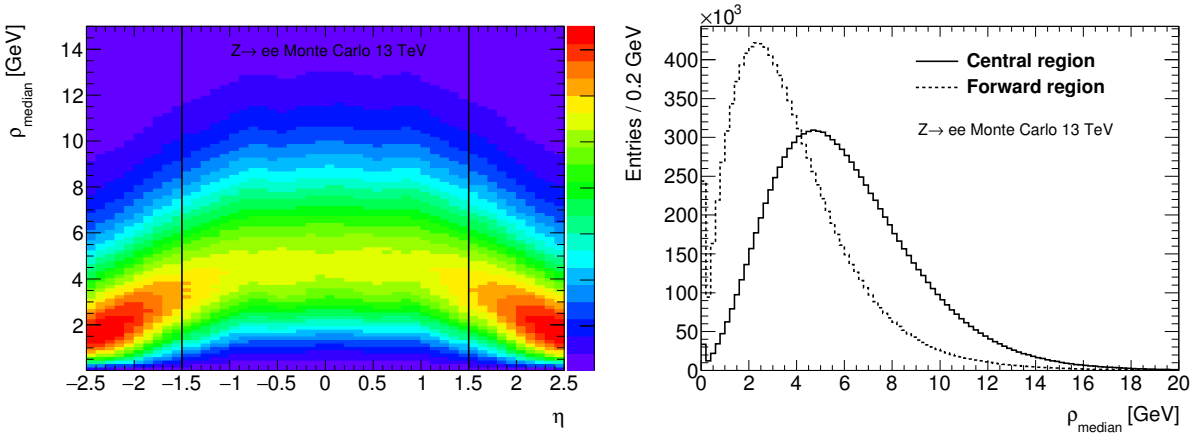

Figure 13: Left: distribution of ρ_{median} as a function of η. Right: distribution of $E_{\mathrm{T,pile-up}}$ in the central and forward regions. Both figures are done for 13 TeV $Z \to e^+e^-$ Monte Carlo events.

The pile-up correction is then evaluated as:

$$E_{\mathrm{T,pile-up}}(\eta) = \rho_{median}(\eta) \times \left(\pi R^2 - A_{\mathrm{core}}\right), \tag{8}$$

where R is the radius of the isolation cone and A_{core} is the area of the core that was subtracted, and corresponds to $5 \times 7 \times 0.025\pi/128$ for the **core57cells** subtraction, $\pi \times 0.1^2$ for the **coreCone** subtraction and is null for the **coreMuon** subtraction.

Finally, the fully corrected isolation is computed as:

$$E_{\text{T,corr}}^{\text{isol}} = E_{\text{T,raw}}^{\text{isol}} - E_{\text{T,core}} - E_{\text{T,leakage}}(p_{\text{T}}) - E_{\text{T,pile-up}}(\eta). \tag{9}$$

4.3 Track isolation

The track isolation, called **ptcone**, is computed by summing the transverse momentum of some selected tracks within a cone centered around the lepton track or photon direction. The selection of the tracks relies on some basic quality cuts on the number of hits, and two cuts $p_{\text{T}} > 1$ GeV, $|z_0 \sin\theta| < 3mm$ [4]) that maximise the fake lepton background in $t\bar{t}$ events (p_{T} cut), and minimize the pile-up dependence of the track isolation ($|z_0 \sin\theta|$ cut).

Oppositely to the calorimeter isolation [5] where a cone with a radius smaller than 0.2 cannot be used, the tiny tracker "cell size" allows to use smaller cone size when needed. For example, in boosted signatures or very busy environments other objects can end up very close to the lepton/photon direction. For such cases, a variable-cone size track isolation, called **ptvarcone**, can be used. For this variable, the cone size gets smaller for larger transverse momentum of the lepton/photon:

$$\Delta R = \min(\frac{k_T}{p_{\text{T}}}, R), \tag{10}$$

where k_T is a constant fixed to 10 GeV and R is the maximum cone size (0.2 to 0.4). In run 1, $k_T = 10$ GeV was optimized on $t\bar{t}$ Monte Carlo events to maximise the background rejection coming from fake leptons.

The cut on $|z_0 \sin\theta|$ aims at selecting tracks that originate from the vertex that is chosen to be the relevant vertex of the process: in most of the cases, the relevant vertex corresponds to the "hardest" vertex of the event, *i.e.* which sum of transverse momenta of the associated tracks is the highest. This is the vertex used by default in the track isolation computation.

In special cases, like the gluon fusion production of a Higgs Boson that decays to two photons without additional jets in the event, where no hard tracks are associated to the process vertex, one can use other information to select the relevant vertex, such as the "pointing" direction coming from the shower shapes of the photon in the calorimeter. In this case, the track isolation needs to be recomputed at analysis level.

The subtraction of the lepton/photon energy from the track isolation is done differently for muons, electrons and converted photons (unconverted photons obviously do not contribute to the track isolation):

- for muons, the track corresponding to the muon is removed.
- for electrons, the association of tracks to the object is done in a more complicated way [23], because electrons can encounter Bremsstrahlung radiation, and the subsequent photons can convert into secondary electrons that should be counted as part of the initial electron energy. Therefore, the tracks are extrapolated to the middle layer of the calorimeter, and all those that fall into a $\Delta\eta = 0.05 \times \Delta\phi = 0.1$ window around the electron cluster position are considered to be part of the electron.
- for converted photons, the track(s) associated to the conversion are removed.

[4] z_0 is the impact parameter of the track along the z axis with respect to the chosen vertex

[5] The lepton/photon cluster has a size of 3×7 or 5×5 in middle cell calorimeter unit of 0.025, which corresponds roughly to a cone of radius 0.1

4.4 Isolation performance

4.4.1 Pile-up resilience

The main justification for switching from the historical isolation variable **etcone** to the new **topoetcone** in 2011 is illustrated on Fig. 14: this shows the evolution of μ_{CB} as a function of the LHC bunch crossing ID (BCID) for 2011 Monte Carlo and data $Z \to ee$ events. **etcone** is corrected from the pile-up by an effective correction as a function of the number of primary vertices in the event, but the remaining large variations show that this correction is not sufficient. The structure observed is a consequence of the bipolar LAr pulse shape. For bunch crossings away from the beginning of the (sub-)trains the cancellation between the in-time crossing and the out-of-time ones is fully efficient and the average cell energy is zero for identical bunch luminosities. On the contrary, near the gaps, the cancellation is only partial : at the beginning of the train, positive contributions add up and the averaged cell energy is positive; at the end of the train, the next would-be filled BCID is missing resulting in a negative offset.

The pile-up correction is much more efficient in the case of **topoetcone** because of the coherent noise suppression in the isolation and in the computation of the energy density used for the pile-up correction, and the isolation is much flatter as a function of the BCID.

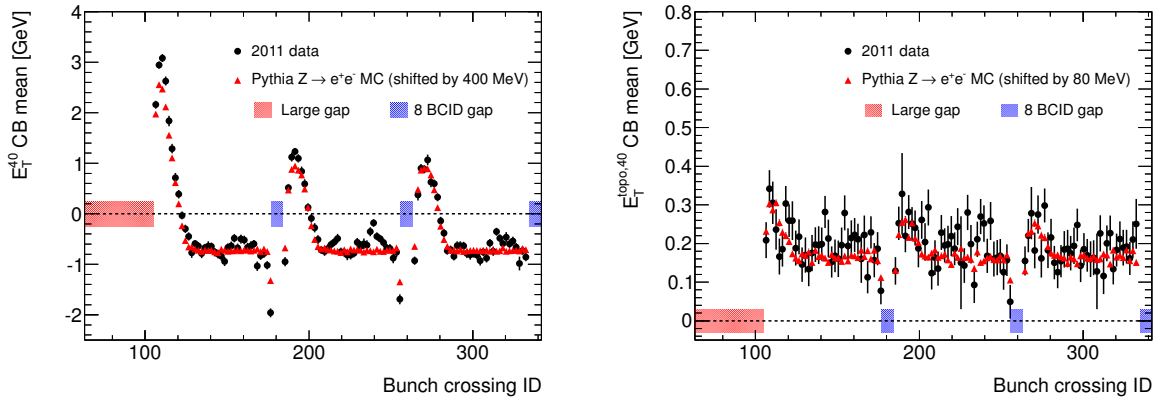

Figure 14: Evolution of μ_{CB} as a function of BCID for **etcone** (left) and **topoetcone** (right) in the 2011 setup. Only the first three sub-trains of the first train are shown.

In 2012, an additional cell-by-cell correction has been introduced as a function of BCID to reduce the residual BCID dependance in Fig. 14. Fig. 15 shows the isolation as a function of the BCID after this cell-by-cell correction has been applied: the bad behavior of **etcone** observed in 2011 data has been corrected, although residual structures are observed, as expected from the Poisson fluctuations of the bunch luminosity. For **topoetcone** the offset subtraction has no dramatic impact since the evolution is flat even if no correction is applied.

Although **etcone** is behaving much better in 2012, there is still a large dependence on pile-up conditions as seen from its evolution as a function of N_{PV}, illustrated in the right plot of Fig. 15, while the **topoetcone** evolution is much flatter.

4.4.2 Data/Monte Carlo agreement

Another argument in favor of **topoetcone** is a better data/Monte Carlo agreement compared to **etcone**, as shown on Fig. 16 for 2011 $Z \to ee$ data and Monte Carlo events. The bottom plots show the ratio of the two distributions after shifting the Monte Carlo to match the data peak. The remaining disagreement for the bulk of the distributions after this simple shift is up to 10% for **etcone**

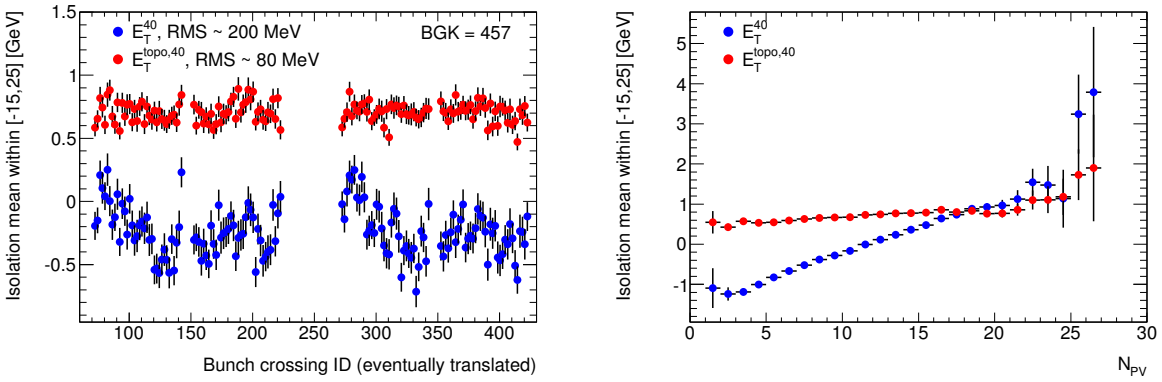

Figure 15: Evolution of **etcone** (E_{T}^{40} blue dots) and **topoetcone** ($E_{\mathrm{T}}^{\mathrm{topo},40}$, red dots) as a function of BCID (left) and as a function of the number of primary vertices (right) in the 2012 setup.

and much reduced for **topoetcone**. This disagreement is most probably due to a bad modeling of the lateral shower shapes of electrons and photons by the ATLAS simulation, and thus a bad modeling of the leakage correction.

Fig. 17 shows the data and Monte Carlo $Z \to ee$ isolation distributions for 2012 8 TeV events, showing again a reasonable agreement.

4.5 Isolation efficiency and scale factor measurement

Most analyses using leptons and photons need to apply some selection cuts on calorimeter and/or track isolation energies (so called isolation working points). The potential disagreement between data and Monte Carlo for these variables may result in different efficiencies for these cuts: the ratio of efficiencies in data and Monte Carlo is called a scale factor.

In run 1, each analysis has been using its own isolation working point and related scale factors and uncertainties. For run 2, there has been a large effort (to which I largely contributed in several aspects) to harmonize the isolation working points and centrally provide the scale factors in the performance (muons and electrons/photons) groups (rather than in each analysis group). This effort is organized by the isolation forum, that I am co-convening since October 2015.

The different techniques available to measure the lepton and photon isolation scale factors are depicted on Fig. 18.

The lepton isolation efficiency can be measured in data using leptons from Z decays, as well as from J/ψ decays, using the infamous Tag and Probe technique that will be described in section 4.5.1.

For photons, the following techniques can be used:

- photons from radiative Z decays: these photons have a low p_{T} (the bulk of events is between 20 and 30 GeV).
- extrapolation from Tag and Probe electron measurements using Monte Carlo.
- inclusive photons after subtracting the background using techniques similar to the Standard Model diphoton analysis described in section 5.

4.5.1 Run 2 isolation working points

Following the model of electron and photon identification, which provides a few working points (typically, “loose”, “medium”, “tight”) for all analyses, we have tried to provide a reduced list of working

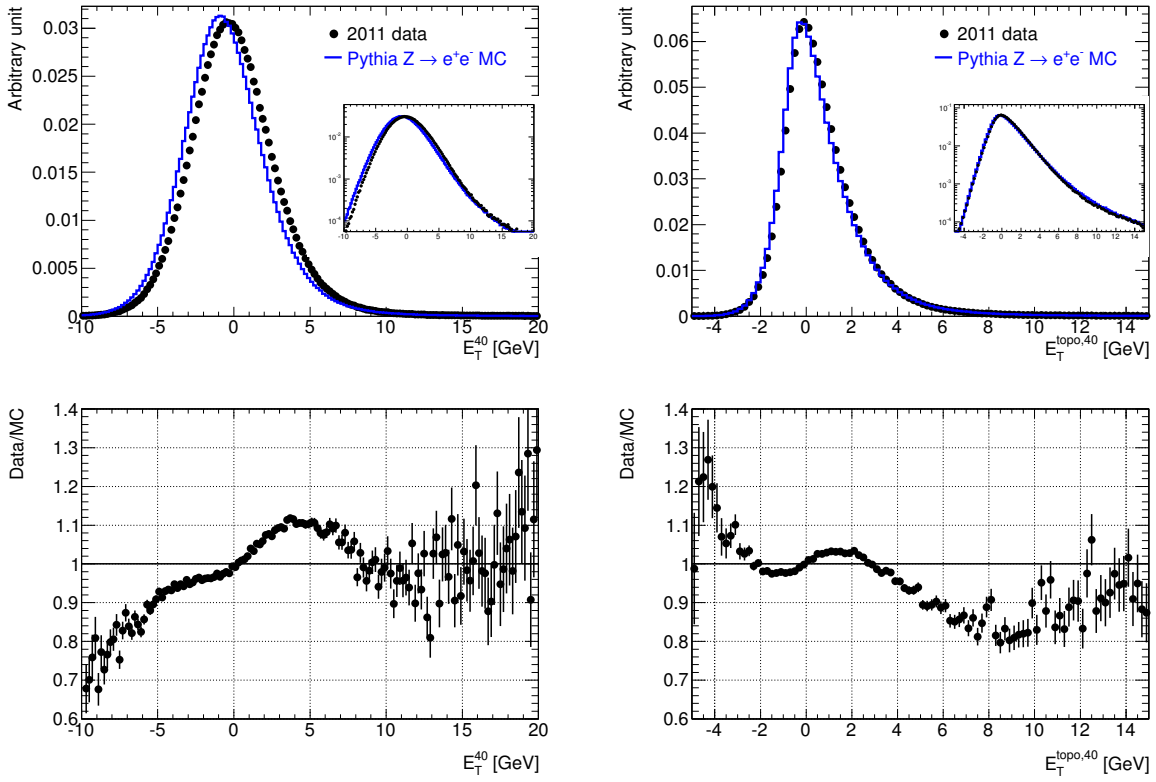

Figure 16: Top : distributions of the **etcone** (left) and **topoetcone** (right) variables for electrons in $Z \to e^+e^-$ events for data (dots) and Pythia MC (histogram). The insert in both plots is simply the distribution shown in logarithmic scale. Bottom : Data over MC ratio as a function of **etcone** (left) and **topoetcone** (right). The MC variables have been shifted before taking the ratio.

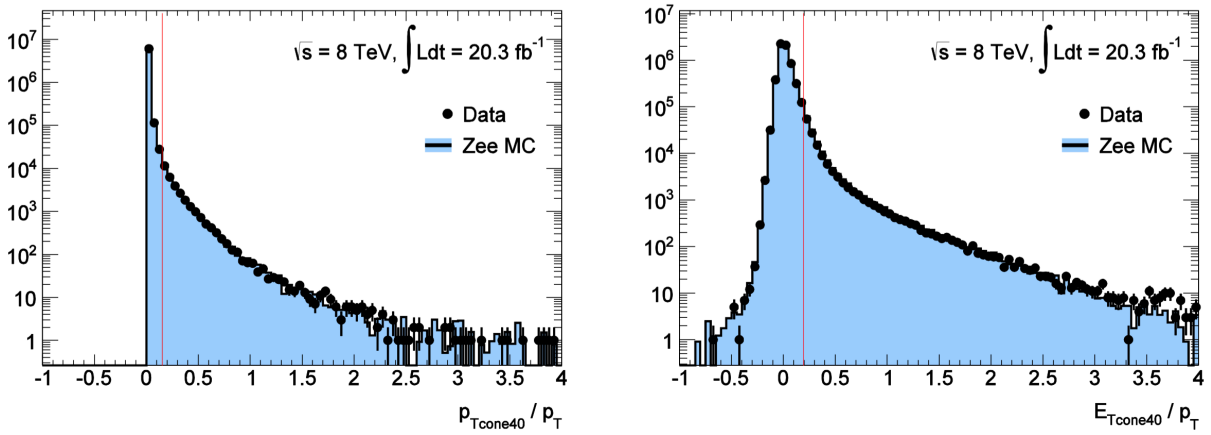

Figure 17: Distributions of **ptcone** (left) and **topoecone** (right) isolation energy (divided by the electron transverse momentum) in 2012 8 TeV $Z \to ee$ data and Monte Carlo.

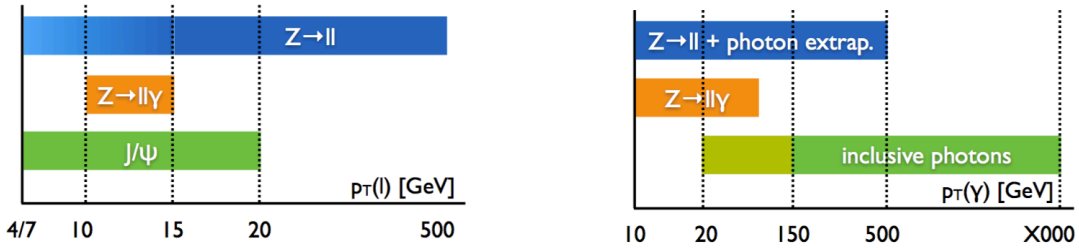

Figure 18: Methods used to compute isolation scale factors for different transverse impulsion ranges for leptons (left) and photons (right). See text for more details.

points for the isolation for run 2. It is nevertheless hopeless to try to reach the same level of simplification as for identification: indeed, the isolation energy is a higher level quantity in the analyses, that is more physics-dependent than the identification. The hope is therefore not to go down to 3 working points, but to around 10.

For these working points to work in a more universal way, one has to choose variables that are not too dependent on the event topology: this is better achieved by using a small cone size like $\Delta R = 0.2$ for the isolation (and in the case of leptons, by using the variable-cone size track isolation **ptvarcone**).

Another potential requirement is to control the efficiency in the entire phase space. It is for example possible to reach a flat efficiency across η and p_{T} by providing different isolation cuts in different bins of η and p_{T}, but at the cost of handling multiple cuts on the isolation. This may be a nice feature for leptons, but can bring complications in the case of photons, where the isolation applied at analysis level needs to be mapped to some theoretical "truth-based" isolation either used in fragmentation photon computations (which works better for isolation cones of at least $\Delta R = 0.4$), or in model-independent fiducial cross-section measurements. In this case, a single cut on the isolation is usually easier to map to the theoretical isolation.

For high p_{T} searches, the isolation is usually required to become very loose at high p_{T} where the backgrounds get much smaller. This is particularly true in the case of the calorimeter isolation, where the leakage correction becomes dominant at large p_{T}: since it is only an averaged correction, and known to not agree well between data and Monte Carlo, the isolation cut needs to be particularly loosened to avoid any unwanted efficiency loss. Looser cuts can be easily obtained by cutting on the relative isolation, *i.e.* isolation divided by p_{T}.

For all these reasons, the lepton official isolation working points are based on **topoetcone20** and **ptvarcone20** variables and provide multiple relative p_{T} cuts to reach a flat efficiency across η and p_{T} over the Z lepton p_{T} range spectrum. The working points are classified according to the target efficiency, *i.e.* 95% (Tight), 99% (Loose) fixed efficiencies, or p_{T}-dependent efficiencies like 90/95% at p_{T} =25 GeV up to 99% at p_{T} =60 GeV(Gradient/GradientLoose). A few "fixed cut" working points (in the form "isolation $<$ a p_{T} + b") are also provided since they are preferred by some analyses.

The photon working points provide single relative p_{T} cuts on **topoetcone** and **ptcone** with a cone size of 0.2 or 0.4 depending on the analysis (a larger cone size being needed for analyses that need photon-related calculators). For the reasons mentioned earlier, only "fixed cut" working points are provided.

4.5.2 Lepton efficiencies: Tag and Probe

The Tag and Probe method consists of using the decay products of a known resonance, such as $Z \to ee$, by selecting an unbiased sample of *e.g.* electrons (called *probes*) after applying strict requirements on the other electron (called *tag*). The efficiency of an isolation working point can then be measured using the probe sample, after subtracting for potential remaining background contamination. The isolation efficiency is usually measured after a number of other requirements have been made on the probe sample, such as the trigger and identification selection. The efficiency measurement thus has to be made for every combination of trigger, identification and isolation working point:

$$\epsilon(\text{isolWP}|\text{trig, ID}) = \frac{N_{\text{trig,ID+isolWP}}}{N_{\text{trig,ID}}}, \tag{11}$$

where $N_{\text{trig,ID}}$ is the number of probe electrons passing a given trigger and identification criterion, and $N_{\text{trig,ID+isolWP}}$ is the number of probe electrons passing also a given isolation working point on top of trigger and identification.

The run 2 electrons "pre-recommendations"

I will describe here the work I did at the beginning of run 2 to settle the Tag and Probe analysis for measuring the isolation scale factors, before the run 2 data arrived. Re-using a part of run 1 data (the so-called "period B" with a luminosity of around 1fb^{-1}) and comparing the behavior of 8 and 13 TeV Monte Carlo, one could thus derive the "pre-recommendations" of isolation scale factors. These have then been updated using the actual run 2 data when they became available: I then co-supervised the student who took over this work from me.

The tag electrons must have $p_{\text{T}} > 25$ GeV, pass various basic quality requirements related to data acquisition and pass the **tightLH** identification criterion [6]. The probe selection is done by requesting that the electrons are in the inner detector acceptance, have at least $p_{\text{T}} > 15$ GeV, pass the basic quality requirements, do not have close-by jets, and pass either the **mediumLH** or **tightLH** identification criteria [7]. The invariant mass of the di-electrons must then satisfy $80 < m_{ee}[\text{ GeV}] < 100$.

The systematic uncertainties on the Tag and Probe method are evaluated by varying the tag selection criteria (**tightLH** identification plus isolation, **mediumLH** identification plus isolation) and the di-electron mass window range. Since the scale factors computed in this analysis were aimed to be used with the first 13 TeV data, which have a few differences with respect to the 8 TeV data (*e.g.* 4 samples are used instead of 5 in the LAr calorimeter data acquisition, there is the additional IBL layer in the inner tracker for run 2 that was not present in run 1, etc...), a additional systematic uncertainty was computed by comparing the 8 TeV data to a 13 TeV Monte Carlo sample (after reweighing the 13 TeV Monte Carlo to the 8 TeV data pile-up).

The di-electron mass spectrum is exploited to subtract the background. A background di-electron mass template is built by reversing some identification and isolation criteria, in order to remove the signal contamination. Alternative reversing cuts are used in order to asses a systematic uncertainty on the background template shape. The background template is then normalized using the high di-electron mass sideband ($100 < m_{ee}[\text{ GeV}] < 250$). This is illustrated on the left plot of Fig. 19 for 2011 run 1 data for all probe electrons without requesting any identification criterion (this corresponds to the denominator of the efficiency measurement for the identification efficiency).

For the isolation efficiency measurement, the denominator already has some identification applied, and the background is much smaller. In particular, when at least the **mediumLH** criterion is applied,

[6] The electron identification for run 2 is done through a likelihood (LH) built from various shower shapes allowing to discriminate real electrons from fake ones. It comprises three levels of identification: **looseLH** (95% efficiency on truth-matched electrons in $Z \to ee$), **mediumLH** (90% efficiency) and **tightLH** ($80 - 85\%$ efficiency).

[7] The **LooseLH** identification criterion will also be considered eventually, but was not for this study.

no background remains in the mass range $80-100$ GeV at all as illustrated on the right plot of Fig. 19. In the case where the **looseLH** identification criterion is applied, then the background subtraction has to be performed, but this is not part of the pre-recommendation study shown here, and will therefore not be further described.

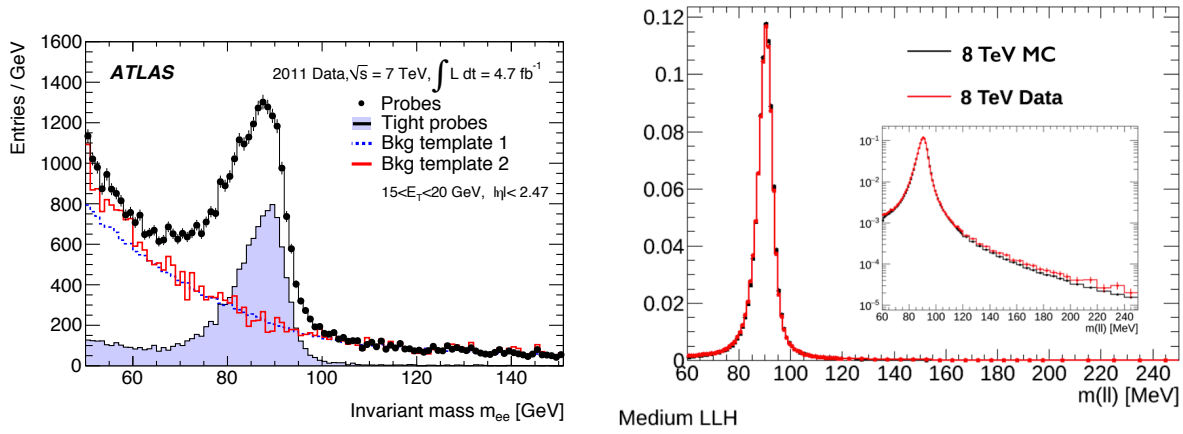

Figure 19: Left: Di-electron mass for the 2011 data and Monte Carlo for events without asking any identification of the probe . Right: Di-electron invariant mass for 8 TeV data and Monte Carlo for events which probe electrons pass the **mediumLH** identification criterion.

Figure 20 shows one example of isolation working point efficiency, the **Loose** isolation working point, for **mediumLH** probe electrons as a function of p_{T}, for the 8 TeV data and Monte Carlo samples, as well as a 13 TeV Monte Carlo sample. The right panel shows the uncertainty on the efficiency measurement, largely dominated by statistics. The systematics uncertainties correspond to those describe above on the Tag and Probe method (variation of tag selection, and di-electron mass window).

Figure 21 shows the efficiency scale factor for the same isolation working point, i.e. the ratio between efficiencies of the 8 TeV data and either the 8 TeV or the 13 TeV Monte Carlo sample. The difference between the 8 and 13 TeV scale factors is eventually the largest systematic uncertainty.

This technique was applied to all lepton working points, and two-dimensional maps in bins of η and p_{T} of scale factors and uncertainties were provided at the beginning of the run 2 data taking. The nominal values of scale factors are those corresponding to the ratio of efficiencies between 8 TeV data and Monte Carlo. The uncertainties are the sum in quadrature of the statistical uncertainty (between 0.15 and 0.3% depending on the isolation working point), the Tag and Probe method systematics (less than 0.05% in all cases) and the difference between 8 and 13 TeV scale factors (dominant uncertainty, between 0.5 and 1%).

Going beyond

The scale factors obtained in the previous section can be applied to analyses that have a similar topology and p_{T} range than the one exploited in the Tag and Probe method, *i.e.* with no close-by objects (either a jet, or other leptons/photons) that could leak into the isolation cone, and in a p_{T} range between 15 and 150 GeV.

A lot of additional work has to be performed for different topologies: in the presence of jets, scale factors can for example be measured as a function of the distance between the lepton/photon and the nearby jet. In the case of multi-leptons or multi-photons signature, one should remove the overlapping lepton/photon from the isolation computation. This was already performed in run 1 analyses in several analyses, but we aim to centrally provide these kinds of corrections for run 2.

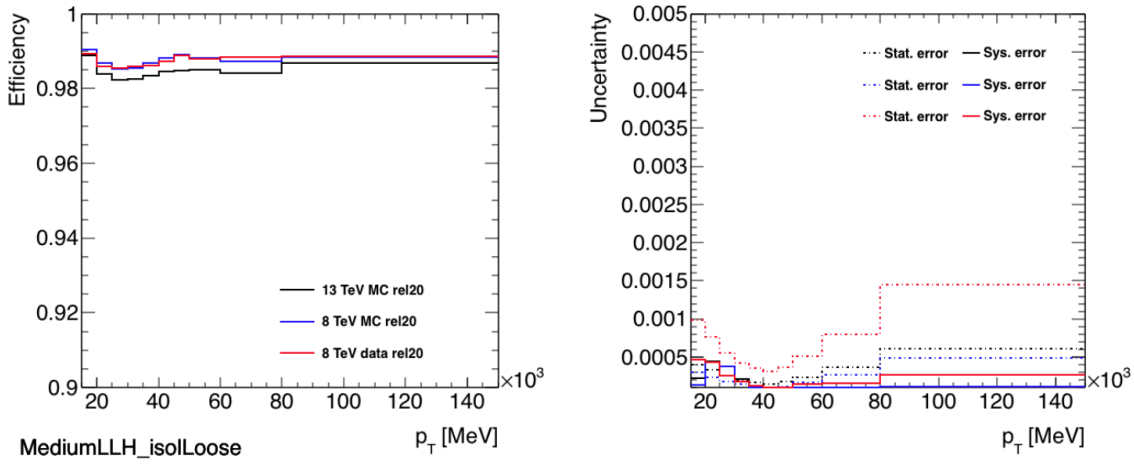

Figure 20: **Loose** isolation working point efficiency for **mediumLH** probe electrons as a function of p_{T}, for the 8 TeV data and Monte Carlo samples, as well as a 13 TeV Monte Carlo sample. The right panel shows the uncertainty on the efficiency measurement, largely dominated by statistics. The systematics uncertainties correspond to those describe in the text on the Tag and Probe method

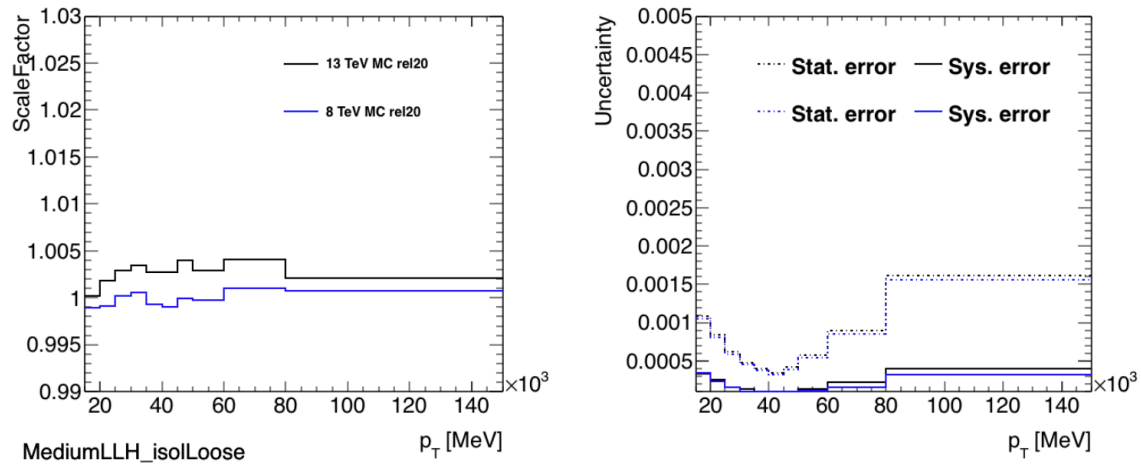

Figure 21: **Loose** isolation working point scale factors for **mediumLH** probe electrons as a function of p_{T}, for the 8 TeV data and Monte Carlo samples, as well as a 13 TeV Monte Carlo sample (left panel - "rel 20" indicates that these samples were reconstructed with the run 2 software ATLAS release). The right panel shows the uncertainty on the efficiency measurement, largely dominated by statistics. The systematics uncertainties correspond to those describe in the text on the Tag and Probe method

One also needs to provide scale factors below 15 GeV and above 150 GeV. The statistics of leptons with $7 < p_T < 15$ GeV is not very high, but can still be used. For the identification efficiency measurement, the lower p_T range (down to 7 GeV) is investigated using J/ψ decays, but this is hardly usable in the case of isolation, because J/ψ are often produced in b-decays, thus yielding non-isolated electrons by nature. Lower p_T's can also be investigated by using radiative Z decays.

For the higher p_T range, most of the high p_T electrons fall into the tail of the Z Breit-Wigner which is harder to describe. Instead, for the identification efficiency measurement, the isolation variable is used to discriminate against the background, but this method clearly can not be used to measure the isolation efficiencies. One idea would be to request high p_T Z's in order to maintain the high p_T electrons in the Z peak, but this will probably rapidly suffer from the lack of statistics, and will anyway have an endpoint in the spectrum when the boosted Z yield too close-by electrons.

4.5.3 Photon efficiencies

I did not provide myself any data-driven measurement of the photon isolation efficiency in run 1, but supervised the related study in the $H \to \gamma\gamma$ group during my convenorship. It is very briefly summarized here, before giving a few insights for run 2.

Run 1 $H \to \gamma\gamma$ photon isolation scale factors

The final state radiation photons from radiative Z decays were exploited in run 1 to provide photon isolation scale factors for the $H \to \gamma\gamma$ analysis.

The left plot of Fig. 22 shows a two-dimensional vue of the di-electron and di-electron plus photon invariant masses. The events peaking at $m(ee\gamma)$ around 90 GeV correspond to the case where the photon was emitted from the final state (FSR photons), while those peaking at $m(ee)$ around 90 GeV to the case where the photon was emitted from the initial state (ISR). The FSR photons can be used in a similar way than in the above Tag and Probe method to measure the photon isolation efficiency in the data, as shown on the right plot of Fig. 22 . The statistics is nevertheless much less than for all $Z \to ee$ events: around 18000 tightly identified photons with $p_T > 15$ GeV are selected in radiative Z decays in the full 8 TeV run 1 dataset, to be compared to more than 15 millions of $Z \to ee$ events (where the probe electron has $p_T > 10$ GeV and is not requested to pass any identification criterion). Therefore, with the run 1 8 TeV statistics, in FSR radiative Z decay photons, one could measure inclusive efficiencies, but not differential ones.

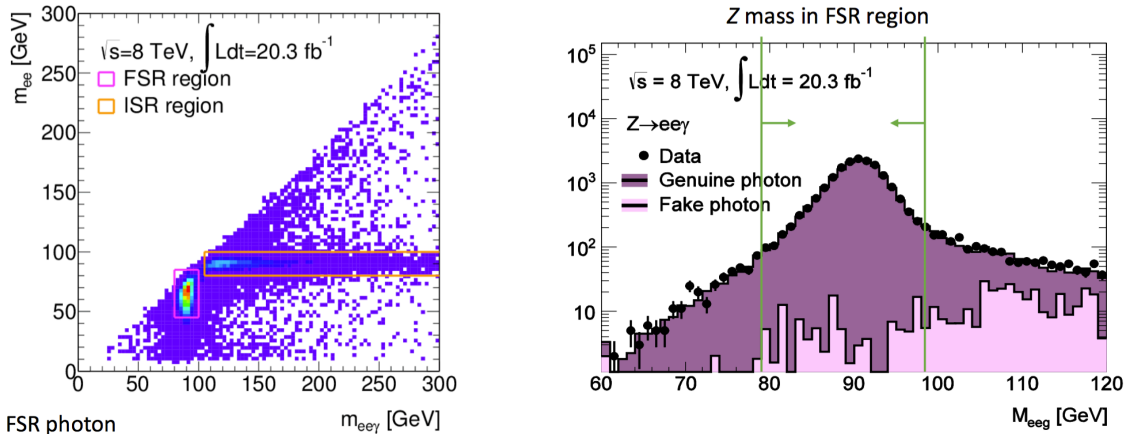

Figure 22: Left: di-electron and di-electron plus photon invariant masses for radiative Z decays. Right: di-electron plus photon invariant mass for FSR events selected as shown in the left plot.

The average p_{T} of selected photons is 23 GeV and the purity is more than 99%. The isolation distributions of **topoetcone40** and **ptcone20** are shown on Fig. 23 and show good agreement between data and Monte Carlo, yielding an inclusive scale factor for the $H \to \gamma\gamma$ isolation cuts (respectively 6 and 2.6 GeV) that differs from one by $SF_{incl} = -0.13 \pm 0.14\%$.

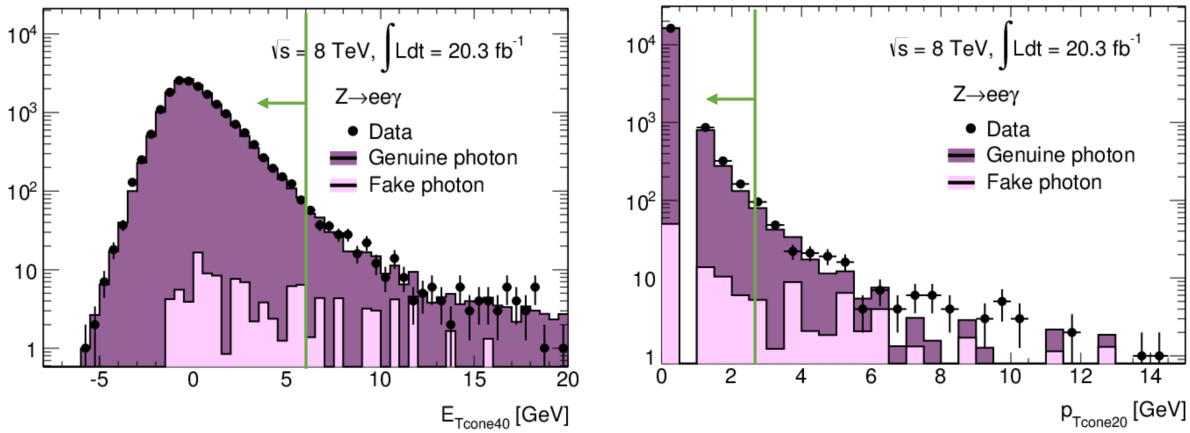

Figure 23: Distribution of **topoetcone40** (left) and **ptcone20** (right) for FSR photons.

This scale factor can nevertheless not be directly applied to the $H \to \gamma\gamma$ analysis for which the average p_{T} of photons is around 60 GeV. The regular Tag and Probe method using electrons was therefore used to measure the variation of inclusive scale factors as a function of p_{T}, where the probe electrons have been reconstructed as unconverted photons. For this purpose, the electron track is not considered, the primary vertex is reconstructed without using this information, and the electron is re-calibrated as an unconverted photon. Fig. 24 shows the resulting distribution, which shows a non-negligible slope as a function of p_{T} of $\alpha = -0.00015 \pm 0.00003$ GeV^{-1}.

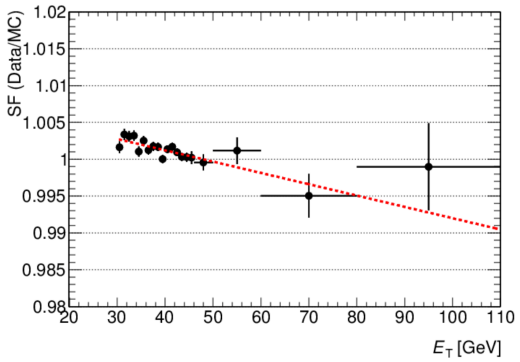

Figure 24: Variation of scale factor as a function of p_{T} using the Z tag and prove method as described in the text.

The scale factors for the efficiencies for the $H \to \gamma\gamma$ analysis are then computed for each photon using this formula:

$$SF(p_T) = SF_{incl} + \alpha\,(p_T - < p_T >_{incl})\,, \tag{12}$$

where SF_{incl} and $< p_T >_{incl}$ are the inclusive scale factor and average photon p_{T} in radiative Z decays and α is the p_{T}-slope measured in Z Tag and Probe. The induced impact on signal yields in each of the analysis categories described in [43] is between 1.3 and 3.8%.

Going beyond

As described in the previous section, the radiative Z decays provide photons with a low p_{T} range, and electrons are still needed to extrapolate the efficiencies to higher p_{T}.

A more copious source of photons can be obtained with an analysis similar to the one described in Sec. 5 (looking for single photons, not photon pairs): direct photons are most of the time isolated, except when they are produced by fragmentation of a parton, or are radiated too close from a parton. These non-isolated photons constitute a background for the measurement of the isolation efficiency of isolated photons such as those from $H \to \gamma\gamma$. Such a measurement will therefore rely on the Monte Carlo modeling of such processes. But inclusive photons can reach a wide p_{T} range, and are copiously produced.

Such an analysis was performed in run 1 to measure corrections to be applied on the isolation in the simulation in order to match the data. This is illustrated on Fig. 25: the left plot shows the isolation distribution adjusted with a background template (measured in the data by reversing some identification cuts) and a signal isolation template taken from the inclusive photon Sherpa simulation. The signal template is allowed to be either shifted (for photons falling into the barrel of the calorimeter) or shifted and smeared (for photons falling into the endcap of the calorimeter): the shift and smearing, shown on the right plot, then constitutes the correction to be applied to the Monte Carlo isolation energy distribution.

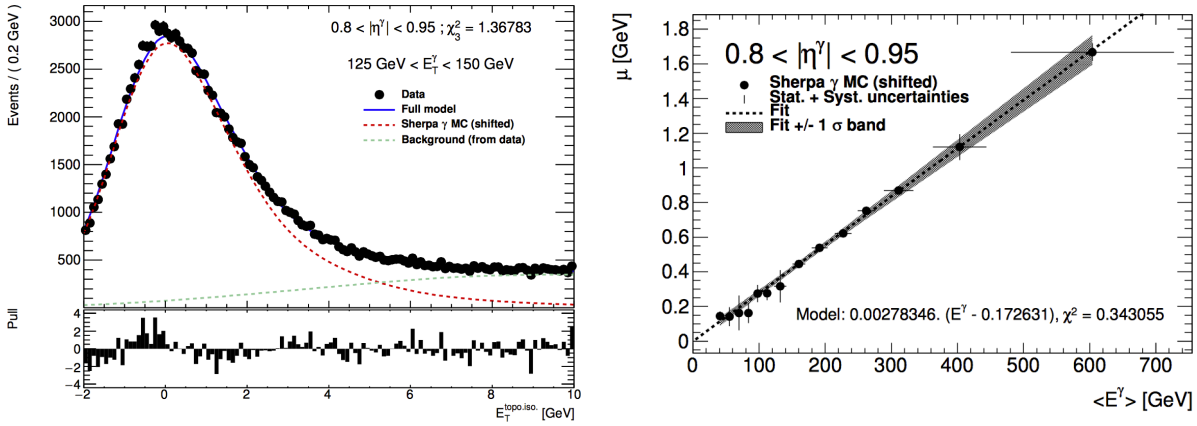

Figure 25: Left: **topoetcone40** distribution in data, adjusted with a data-driven background template, and a signal template from the inclusive photon Sherpa simulation, allowing for a potential shift (or shift+smearing in the case of endcap photons). Right: shift on the signal template as a function of the p_{T} of the photon in a given η bin.

Eventually, such an analysis can also be used to measure the photon isolation efficiency, after taking care of the non-isolated photon component. This technique will be further developed in run 2.

5 Measurement of isolated photon pair production at $\sqrt{s}$=7 TeV

The isolation energy is a key variable to study the main $H \to \gamma\gamma$ background: the direct photon pair production. At the beginning of run 1, I studied this process in detail: the measurement of the inclusive and differential cross-sections for this process allows to test the various theoretical predictions available. This kind of study then allows to choose the best generator to produce background samples used in the $H \to \gamma\gamma$ analysis, in particular to help choosing a proper analytical function to model the $m_{\gamma\gamma}$ spectrum.

Usually, such precision measurements of Standard Model processes take time, and therefore, only 7 TeV data-related measurements have been published in ATLAS so far. There were two such publication: one using 37 pb^{-1} [24] for which I was one of the main analyzers and editors, and one using the full 7 TeV statistics (4.9 fb^{-1}) [25] for which I was also one of the main analysers. I will describe here shortly the second analysis, for which my main contribution consisted in developing the two dimensional sidebands and fit methods to extract the jet backgrounds and the related systematic uncertainties.

5.1 Introduction

In this analysis, the production cross section for two isolated photons with transverse energies (E_{T}) above 25 GeV and 22 GeV respectively, in the acceptance of the ATLAS electromagnetic calorimeter ($|\eta| < 1.37$ and $1.52 < |\eta| < 2.37$) and with an angular separation $\Delta R > 0.4$, is measured.

The integrated di-photon production cross section is measured, as well as the differential cross sections as a function of four kinematic variables: the di-photon invariant mass ($m_{\gamma\gamma}$), the di-photon transverse momentum ($p_{\mathrm{T},\gamma\gamma}$), the azimuthal separation between the photons in the laboratory frame ($\Delta\phi_{\gamma\gamma}$), and the cosine of the polar angle of the highest E_{T} photon in the Collins–Soper di-photon rest frame ($\cos\theta^*_{\gamma\gamma}$) [26]. The first distribution is of obvious interest for resonance searches; the second and the third provide important information in the study of higher-order QCD perturbative effects and fragmentation, especially in some specific regions such as the small $\Delta\phi_{\gamma\gamma}$ limit; the fourth is used to investigate the spin of di-photon resonances.

The results are compared to the predictions from: parton-shower Monte Carlo generators, Pythia 6.4.21 [27] and Sherpa 1.3.1 [28]; parton-level calculations with next-to-leading-order (NLO) QCD corrections using the Diphox [29] program complemented by gamma2mc [30]; and at next-to-next-to-leading-order (NNLO), using 2γNNLO [31].

5.2 Event Selection

Events are collected using a di-photon trigger with a nominal transverse energy threshold of 20 GeV for both photon candidates.

Photons are reconstructed from electromagnetic energy clusters in the calorimeter and tracking information provided by the ID as described in ref. [32]. The cluster energies are corrected using an in-situ calibration based on the Z boson mass peak [33]. In order to benefit from the fine segmentation of the first layer of the electromagnetic calorimeter to discriminate between genuine prompt photons and fake photons within jets, the photon candidate pseudorapidity must satisfy $|\eta| < 1.37$ or $1.52 < |\eta| < 2.37$. We retain photon candidates passing loose identification requirements, based on the same shower shape variables – computed with better granularity and resolution – and the same thresholds used at trigger level. The highest-E_{T} ("leading") and second highest-E_{T} ("subleading") photons within the acceptance and satisfying the loose identification criteria are required to have $E_{\mathrm{T},1} > 25$ GeV and $E_{\mathrm{T},2} > 22$ GeV, respectively. The angular separation between the two photons, $\Delta R =$

$\sqrt{(\Delta\eta)^2 + (\Delta\phi)^2}$, is required to be larger than 0.4, in order to avoid one photon candidate depositing significant energy in the isolation cone of the other, as defined below.

Two further criteria are used to define the signal and background control regions: the tight photon selection [32] (abbreviated as **T** in the following), corresponding to requirements on nine discriminating variables computed from the energy leaking into the HCAL and the lateral and longitudinal shower development in the ECAL, and the topological isolation energy $E_{\mathrm{T}}^{\mathrm{iso}}$(described in section 4);

Signal photons are required to pass the tight selection ("tight photons") and the isolation requirement **I**, $-4 < E_{\mathrm{T}}^{\mathrm{iso}} < 4$ GeV. A total of 165 767 pairs of tight, isolated photons are selected. The non-tight ($\tilde{\mathbf{T}}$) photon candidates are defined as those failing the tight criteria for at least one of the shower-shape variables that are computed from the energy deposits in a few cells of the first layer of the electromagnetic calorimeter adjacent to the cluster barycentre. Photon candidates with $4 < E_{\mathrm{T}}^{\mathrm{iso}} < 8$ GeV are considered non-isolated ($\tilde{\mathbf{I}}$).

5.3 Signal yield extraction

After the selection, the main background is due primarily to γ-jet and secondarily to di-jet (jj) final states, collectively called "jet background" in the following. A small residual background contamination arises from events where isolated electrons are misidentified as photons.

Both the two-dimensional sidebands and the two-dimensional fit methods use the photon transverse isolation energy and the tight identification criteria to discriminate prompt photons from jets. They rely on the fact that the correlations between the isolation and the tight criteria in background events are small, and that the signal contamination in the non-tight or non-isolated control regions is low.

The two-dimensional sidebands method counts the numbers of photon candidate pairs where each of the candidates passes or fails the tight and the isolation criteria. Four categories are defined for each photon, resulting in 16 categories of events. The inputs to the method are the numbers of events in the categories and the signal efficiencies of the tight and isolation requirements. The correlation between these two requirements is assumed to be negligible for background events. The method allows the simultaneous extraction of the numbers of true di-photon signal, γj, jγ[8] and jj background events, and the tight and isolation efficiencies for fake photon candidates from jets ("fake rates"). The expected number of events in each category is written as a function of the parameters (yields, efficiencies, fake rates and correlation factors) and the system of 16 equations is solved with a χ^2 minimization procedure. This method allows the extraction of different isolation fake rates for jets in jγ or jj events as well as a correlation factor for the isolation of jet pairs.

The two-dimensional fit method consists of an extended maximum likelihood template fit to the two-dimensional distribution of the transverse isolation energies $E_{\mathrm{T},1}^{\mathrm{iso}}$ and $E_{\mathrm{T},2}^{\mathrm{iso}}$ of the two photon candidates in events belonging to the **T**-**T** sample, *i.e.* where both photons satisfy the tight identification criteria. The fit is performed in the isolation range $-4 < E_{\mathrm{T},i}^{\mathrm{iso}} < 8$ GeV ($i = 1, 2$). The correlations between the transverse isolation energies of the two candidates in di-photon, γj, and jγ events are found to be negligible in MC samples, and the products of two one-dimensional templates for $E_{\mathrm{T},1}^{\mathrm{iso}}$ and $E_{\mathrm{T},2}^{\mathrm{iso}}$ are used for each of the three event species. For the jj component, large correlations are observed in data, and a two-dimensional template is used.

The transverse isolation energy distributions of the signal photons and the corresponding efficiencies of the signal requirement $-4 < E_{\mathrm{T}}^{\mathrm{iso}} < 4$ GeV are obtained from the SHERPA di-photon sample, separately for the leading and the subleading candidates. In the two-dimensional fit method, the templates are shifted by +160 and +120 MeV respectively in order to maximize the likelihood, as determined from a scan as a function of the shifts. These values are also used to compute the signal

[8] Here and in the following, γj (jγ) denotes the events where the leading (subleading) candidate is a true photon, and the other candidate a true jet.

efficiencies of the isolation requirement needed in the two-dimensional sidebands method. Shifts of similar size between ATLAS data and MC simulation have been observed in the transverse isolation energy distribution, computed with the same technique (based on topological clusters inside a cone of radius 0.4), of electron control samples selected from $Z \to ee$ decays with a tag-and-probe method.

The $E_{\mathrm{T}}^{\mathrm{iso}}$ distributions of prompt photons in γj and jγ events are assumed to be identical to that of prompt photons in di-photon events, as found in simulated samples. The tight identification efficiencies for prompt photons, needed in the two-dimensional sidebands method and in the final cross section measurement, are estimated using the same di-photon MC sample. The shower shape variables are corrected for the observed differences between data and simulation in photon-enriched control samples. Residual differences between the efficiencies in the simulation and in data are corrected using scale factors determined from control samples of photons from radiative Z boson decays, electrons selected with a tag-and-probe technique from $Z \to ee$ decays, and photon-enriched control samples of known photon purity [34]. After applying these corrections, the photon identification efficiency in the simulation is estimated to reproduce the efficiency in data to within 2%. For the two-dimensional fit, the transverse isolation energy template of the leading (subleading) jet in jγ (γj) events is extracted directly from data where one candidate passes the non-tight and the other passes both the tight identification and isolation (**TI**) requirements. For jj events, the two-dimensional template is obtained from data in which the two candidates are required to be non-tight. The correlation is found to be about 8%. The jet background templates are corrected for signal leakage in the control samples, estimated from the SHERPA sample.

Figure 26 shows the projections of the two-dimensional fit to the transverse isolation energies of the leading and subleading photon candidates. The yields for each of the four components extracted with the two-dimensional sidebands method and the two-dimensional fit are given in table 2. The di-photon purity is around 68% and the di-photon yields agree within 1.5% between the two methods.

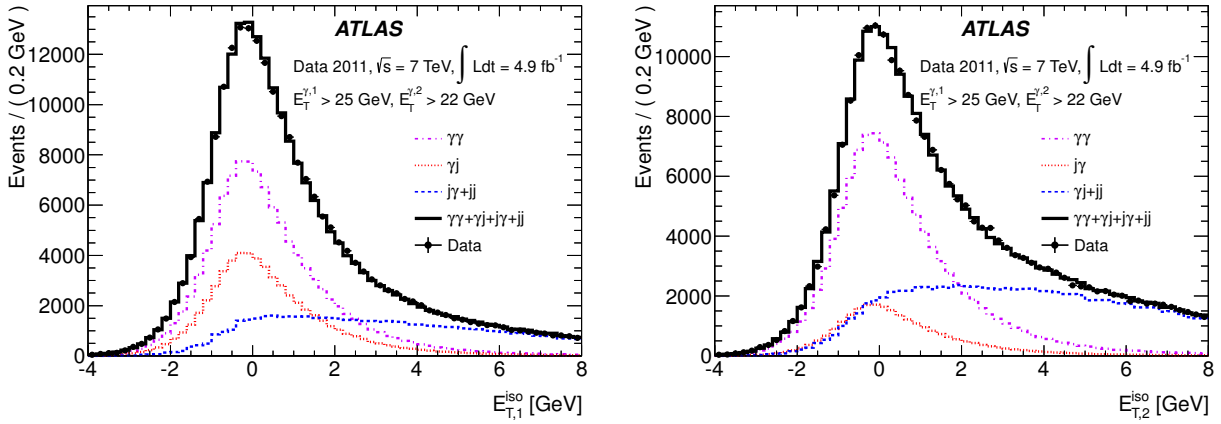

Figure 26: Projections of the two-dimensional fit to the transverse isolation energies of the two photon candidates: leading photon (left) and sub-leading photon (right). The photon templates from SHERPA are shifted by +160 MeV (+120 MeV) for the leading (subleading) photon. Solid circles represent the observed data. The (black) solid line is the fit result, the (violet) dash-dotted curve shows the $\gamma\gamma$ component. The (red) dotted line shows in the left (right) figure the contribution from γj (jγ) events. In both figures, the (blue) dashed line represents a broad background component in the photon candidates' sample: for the leading candidate this is due to jγ and jj final states, whereas for the sub-leading candidate it comes from γj and jj final states.

To obtain the differential signal yields as a function of the di-photon kinematic variables, such as $m_{\gamma\gamma}$, $p_{\mathrm{T},\gamma\gamma}$, $\Delta\phi_{\gamma\gamma}$ and $\cos\theta^*_{\gamma\gamma}$, the above methods are applied in each bin of the variables. Figure

Yield	two-dimensional sidebands results			two-dimensional fit results		
$N_{\gamma\gamma}$	113 200	$\pm$600 (stat.)	$^{+5000}_{-8000}$ (syst.)	111 700	$\pm$500 (stat.)	$^{+4500}_{-7600}$ (syst.)
$N_{\gamma j}$	31 500	$\pm$400 (stat.)	$^{+3900}_{-3100}$ (syst.)	31 500	$\pm$300 (stat.)	$^{+4800}_{-3600}$ (syst.)
$N_{j\gamma}$	13 000	$\pm$300 (stat.)	$^{+2500}_{-\ 800}$ (syst.)	13 900	$^{+300}_{-200}$ (stat.)	$^{+3400}_{-2100}$ (syst.)
N_{jj}	8 100	$\pm$100 (stat.)	$^{+1900}_{-1400}$ (syst.)	8 300	$\pm$100 (stat.)	$^{+\ 300}_{-2100}$ (syst.)

Table 2: Total yields for two candidates satisfying the tight identification and the isolation requirement $-4 < E_{\mathrm{T}}^{\mathrm{iso}} < 4$ GeV. Both statistical and total systematic uncertainties are listed.

27 shows the differential spectra of the signal and background components obtained with the two-dimensional fit. In some regions of the di-photon spectra, discrepancies with the two-dimensional sidebands results are larger than those observed for the integrated yield. The results from the two-dimensional fit are used to extract the nominal cross sections, while differences between the results obtained with the two methods are included in the final systematic uncertainty.

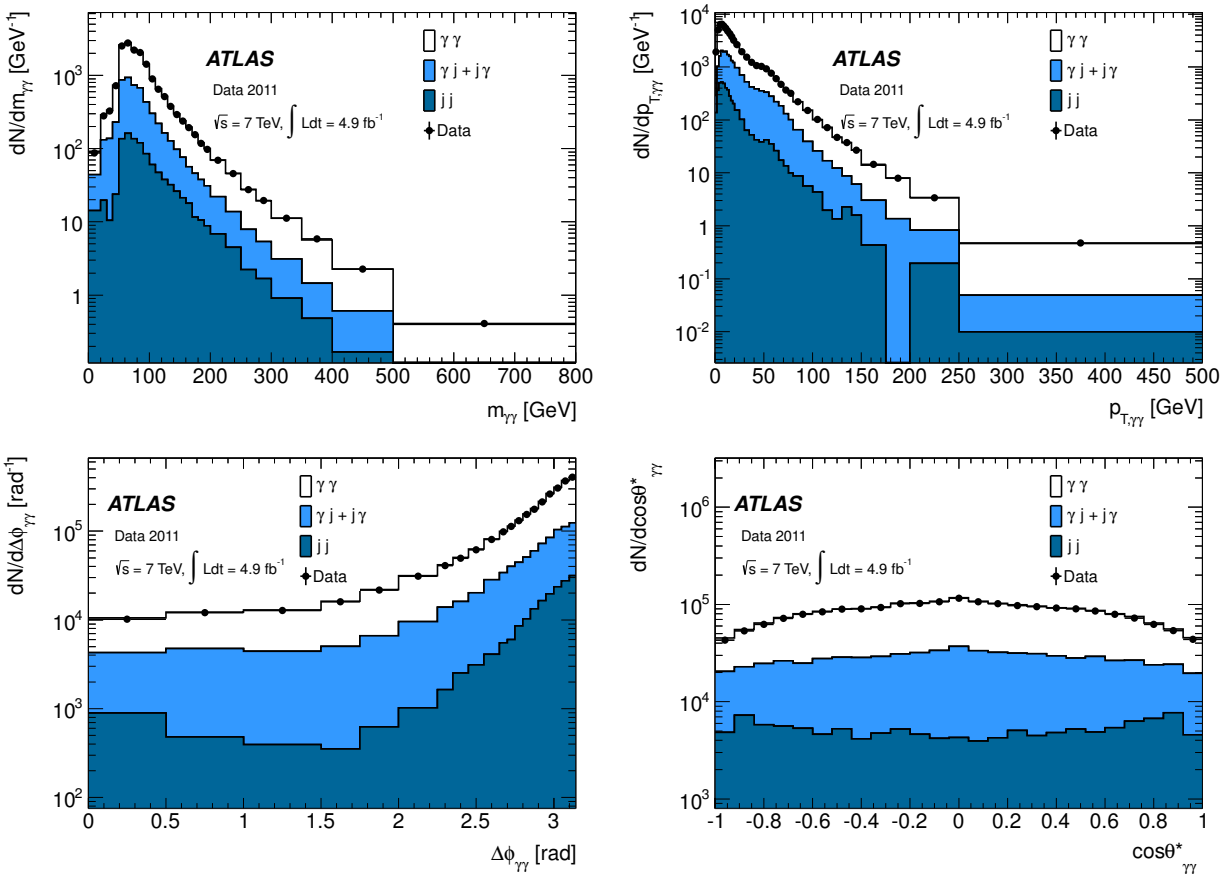

Figure 27: Differential spectra in data (solid circles) and from the two-dimensional fit, for the $\gamma\gamma$ (hollow histogram), γj+jγ (light solid histogram), and jj (dark solid histogram) contributions. The spectra are shown for the following di-photon variables: $m_{\gamma\gamma}$ (top left), $p_{\mathrm{T},\gamma\gamma}$ (top right), $\Delta\phi_{\gamma\gamma}$ (bottom left), $\cos\theta^*_{\gamma\gamma}$ (bottom right).

Several sources of systematic uncertainty on the signal yield, estimated after the jet background subtraction, are considered.

The dominant uncertainty originates from the choice of the background control regions and accounts for both the uncertainty on the background transverse isolation energy distribution and its correlation with the identification criteria. It is first estimated by varying the number of relaxed criteria in the non-tight definition, yielding a systematic uncertainty of ±9%.

In the nominal result, the photon isolation templates are taken from the SHERPA di-photon sample. A systematic uncertainty is evaluated by using alternative templates from the PYTHIA di-photon sample, and from data, yielding a systematic uncertainty between 2 to 4%.

Other systematic effects have been considered (such as the bias created by neglecting the dependence of the identification and isolation efficiencies on η and E_{T}, the effect of assuming identical templates for photons in di-photon and in γ-jet events, the uncertainty on the shifts applied to the MC photon templates, the impact of the identification efficiencies on the signal leakage correction, ...) and are found to be smaller than those previously discussed.

5.4 Cross-section extraction

This section describes the extraction of the final cross sections. The background-subtracted differential spectra are first unfolded to the generated-particle level, to take into account reconstruction and selection efficiencies estimated from the simulation, and then divided by the integrated luminosity of the data sample and the trigger efficiency relative to the offline selection.

5.4.1 Efficiency and unfolding

The background-subtracted differential distributions obtained from the data are unfolded to obtain the particle-level spectra by dividing the signal yield in each bin of the di-photon observable under study by a "bin-by-bin" correction, which accounts for signal reconstruction and selection efficiencies and for finite resolution effects. The bin-by-bin nominal corrections are evaluated from the SHERPA di-photon simulated sample as the number of simulated di-photon events satisfying the selection criteria (excluding the trigger requirement) and for which the reconstructed value of the variable X under consideration is in bin i, divided by the number of simulated di-photon events satisfying the nominal acceptance criteria at generator-level and for which the generated value of X is in the same bin i. The generator-level photon transverse isolation energy is computed from the true four-momenta of the generated particles (excluding muons and neutrinos) inside a cone of radius 0.4 around the photon direction. The pileup contribution is removed using an analogous method to the one for the experimental isolation variable, by subtracting the product of the area of the isolation cone and the median transverse energy density of the low-transverse-momentum truth-particle jets.

5.5 Results

The differential cross sections as a function of $m_{\gamma\gamma}$, $p_{\mathrm{T},\gamma\gamma}$, $\Delta\phi_{\gamma\gamma}$, and $\cos\theta^*_{\gamma\gamma}$ are extracted following the unfolding procedure described in section 5.4.1.

The integrated cross section is measured by dividing the global $\gamma\gamma$ yield (obtained after subtracting the electron contribution from the two-dimensional fit result in table 2) by the product of the average event selection efficiency (from the simulation), trigger efficiency and integrated luminosity.

The selection efficiency is defined as the number of reconstructed simulated di-photon events satisfying the detector-level selection criteria divided by the number of generated events satisfying the equivalent truth-level criteria, thus correcting for reconstructed events with true photons failing the acceptance cuts. It is computed from simulated di-photon events, reweighting the spectrum of one of the four di-photon variables under study in order to match the differential background-subtracted di-photon spectrum observed in data. Choosing different variables for the reweighting

of the simulated events leads to slightly different but consistent efficiencies, with an average value of 49.6% and an RMS of 0.2%. Including systematic uncertainties on the photon reconstruction and identification efficiencies, from the same sources described in section 5.4.1, the event selection efficiency is estimated to be $49.6^{+1.9}_{-1.7}$%. The dominant contributions to the efficiency uncertainty are from the photon identification efficiency uncertainty (±1.2%), the energy scale uncertainty ($^{+1.2}_{-0.5}$%), and the choice of the MC generator and the detector simulation (±0.9%). Negligible uncertainties are found to arise from the energy resolution, the isolation requirement (evaluated by shifting the isolation variable by the observed data–MC difference) and from the different pile-up dependence of the efficiency in data and MC simulation.

The obtained integrated cross section is $44.0^{+3.2}_{-4.2}$ pb, where the dominant uncertainties are the event selection efficiency and the jet subtraction systematic uncertainties.

5.6 Comparison with theoretical predictions

The results are compared both to fixed-order NLO and NNLO calculations, obtained with parton-level MC generators (DIPHOX+GAMMA2MC and 2γNNLO), and to the generated-particle-level di-photon spectra predicted by leading-order (LO) parton-shower MC generators used in the ATLAS full simulation (PYTHIA and SHERPA).

The main differences between the four predictions are the following:

- 2γNNLO provides a NNLO calculation of the direct part of the di-photon production cross section, but neglects completely the contribution from the fragmentation component, where one or both photons are produced in the soft collinear fragmentation of coloured partons.

- DIPHOX provides a NLO calculation of both the direct and the fragmentation parts of the di-photon production cross section. It also includes the contribution from the box diagram ($gg \to \gamma\gamma$), which is in principle a term of the NNLO expansion in the strong coupling constant α_s, but – due to the large gluon luminosity at the LHC – gives a contribution comparable to that of the LO terms. For these reasons, higher-order contributions to the box diagrams, technically at NNNLO but of size similar to that of NLO terms, are also included in our calculation by using GAMMA2MC.

- PYTHIA provides LO matrix elements for di-photon production and models the higher-order terms through γ-jet and di-jet production in combination with initial-state and/or final-state radiation. It also features parton showering and an underlying event model;

- SHERPA has features similar to those of PYTHIA, and in addition includes the di-photon higher-order real-emission matrix elements. For this study, up to two additional QCD partons are generated.

The nominal factorization (μ_F), renormalization (μ_R), and – in the case of DIPHOX and GAMMA2MC – fragmentation (μ_f) scales are set in all cases to the di-photon invariant mass, $m_{\gamma\gamma}$. The theoretical uncertainty error bands for PYTHIA and SHERPA include only statistical uncertainties. The theory uncertainty error bands for the NLO and NNLO predictions include in addition PDF and scale uncertainties. PDF uncertainties are estimated by varying each of the eigenvalues of the PDFs by $\pm1\sigma$ and summing in quadrature separately positive and negative variations of the cross section. For DIPHOX and GAMMA2MC, scale uncertainties are evaluated by varying each scale to $m_{\gamma\gamma}/2$ and $2m_{\gamma\gamma}$, and the envelope of all variations is taken as a systematic error; the final uncertainty is dominated by the configurations in which the scales are varied incoherently. For 2γNNLO, the scale uncertainty is evaluated by considering the variation of the predicted cross sections in the two cases $\mu_R = m_{\gamma\gamma}/2$, $\mu_F = 2m_{\gamma\gamma}$ and $\mu_R = 2m_{\gamma\gamma}$, $\mu_F = m_{\gamma\gamma}/2$.

Both PYTHIA and SHERPA are expected to underestimate the total cross section, because of the missing NLO (and higher-order) contributions. At low $p_{\mathrm{T},\gamma\gamma}$ and for $\Delta\phi_{\gamma\gamma}$ near π where multiple soft gluon emission is important, PYTHIA and SHERPA are expected to better describe the shape of the differential distributions, thanks to the effective all-order resummation of the leading logs performed by the parton shower. On the other hand, in the same regions fixed-order calculations are expected to exhibit infrared divergences. Finally, 2γNNLO is expected to underestimate the data in regions populated by the contribution from fragmentation (low $\Delta\phi_{\gamma\gamma}$ and $m_{\gamma\gamma}$, and $\cos\theta^*_{\gamma\gamma}\approx 1$).

The total cross section estimated by PYTHIA and SHERPA with the ATLAS simulation settings is 36 pb, and underestimates the measured cross section by 20%. The DIPHOX+GAMMA2MC total cross section is 39^{+7}_{-6} pb and the 2γNNLO total cross section is 44^{+6}_{-5} pb, where the uncertainty is dominated by the choice of the nominal scales.

The comparisons between the experimental cross sections and the predictions by PYTHIA and SHERPA are shown in figure 28. In order to compare the shapes of the MC differential distributions to the data, their cross sections are rescaled by a factor 1.2 to match the total cross section measured in data. PYTHIA misses higher order contributions, as clearly seen for low values of $\Delta\phi_{\gamma\gamma}$, but this is compensated by the parton shower for $\Delta\phi_{\gamma\gamma}$ near π and at low $p_{\mathrm{T},\gamma\gamma}$. It is worth noting that the shoulder expected (and observed) in the $p_{\mathrm{T},\gamma\gamma}$ cross section around the sum of the E_{T} thresholds of the two photons is almost absent in PYTHIA, while SHERPA correctly reproduces the data in this region. This is interpreted as being due to the additional NLO contributions in SHERPA combined with differences in the parton showers. Overall, SHERPA reproduces the data rather well, except at large $m_{\gamma\gamma}$ and large $|\cos\theta^*_{\gamma\gamma}|$.

The comparisons between the data cross sections and the predictions by 2γNNLO and DIPHOX+GAMMA2MC are shown in figure 29. In the $\Delta\phi_{\gamma\gamma} \simeq \pi$, low $p_{\mathrm{T},\gamma\gamma}$ region, DIPHOX+GAMMA2MC fails to match the data. This is expected because initial-state soft gluon radiation is divergent at NLO, without soft gluon resummation. Everywhere else DIPHOX+GAMMA2MC is missing NNLO contributions and clearly underestimates the data.

With higher order calculations included, 2γNNLO is very close to the data within the uncertainties. However, the excess at $\Delta\phi_{\gamma\gamma} \simeq \pi$ and low $p_{\mathrm{T},\gamma\gamma}$ is still present, as expected for a fixed-order calculation. Since the fragmentation component is not calculated in 2γNNLO, the data is slightly underestimated by 2γNNLO in the regions where this component is larger: at low $\Delta\phi_{\gamma\gamma}$, low mass, intermediate $p_{\mathrm{T},\gamma\gamma}$ (between 20 GeV and 150 GeV) and large $|\cos\theta^*_{\gamma\gamma}|$.

5.6.1 Conclusions

The measurement described above is the first measurement of the cross-section for the production of isolated-photon pairs in the ATLAS experiment and served several goals:

- the confrontation of the measured cross-sections with several theoretical predictions allowed to disentangle these different predictions and chose the most appropriate ones for the LHC regime.
- the analysis techniques developed for this measurement were then widely used in ATLAS to perform photon-samples related background decompositions: this is the case for example in the Higgs Boson search in its diphoton decay, in order to produce a realistic background simulation with the correct admixtures of di-photon, photon-jet and di-jet components. The background fitting for the Higgs Boson search can then be exercised on this realistic background simulation.
- these techniques can also be used to measure the data-Monte Carlo agreement for the isolation energy variable, and thus assess scale factors for the isolation efficiencies.

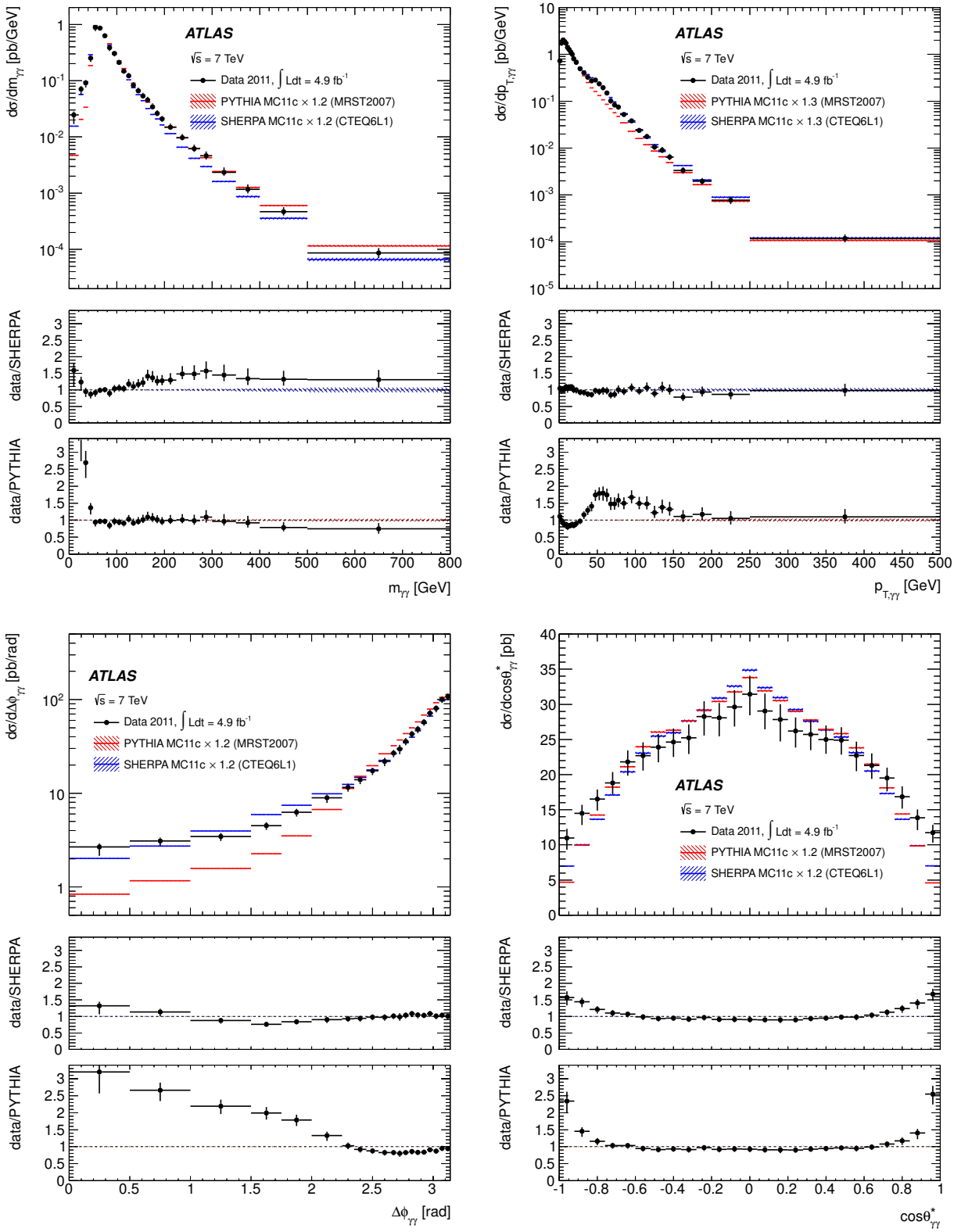

Figure 28: Comparison between the experimental cross sections and the predictions obtained with parton-shower LO simulations: $m_{\gamma\gamma}$ (top left), $p_{\mathrm{T},\gamma\gamma}$ (top right), $\Delta\phi_{\gamma\gamma}$ (bottom left), $\cos\theta^*_{\gamma\gamma}$(bottom right). The LO cross sections have been scaled to the total data cross section, by a factor 1.2. Black dots correspond to data with error bars for their total uncertainties, which are dominated by the systematic component. The simulated cross sections include only statistical uncertainties.

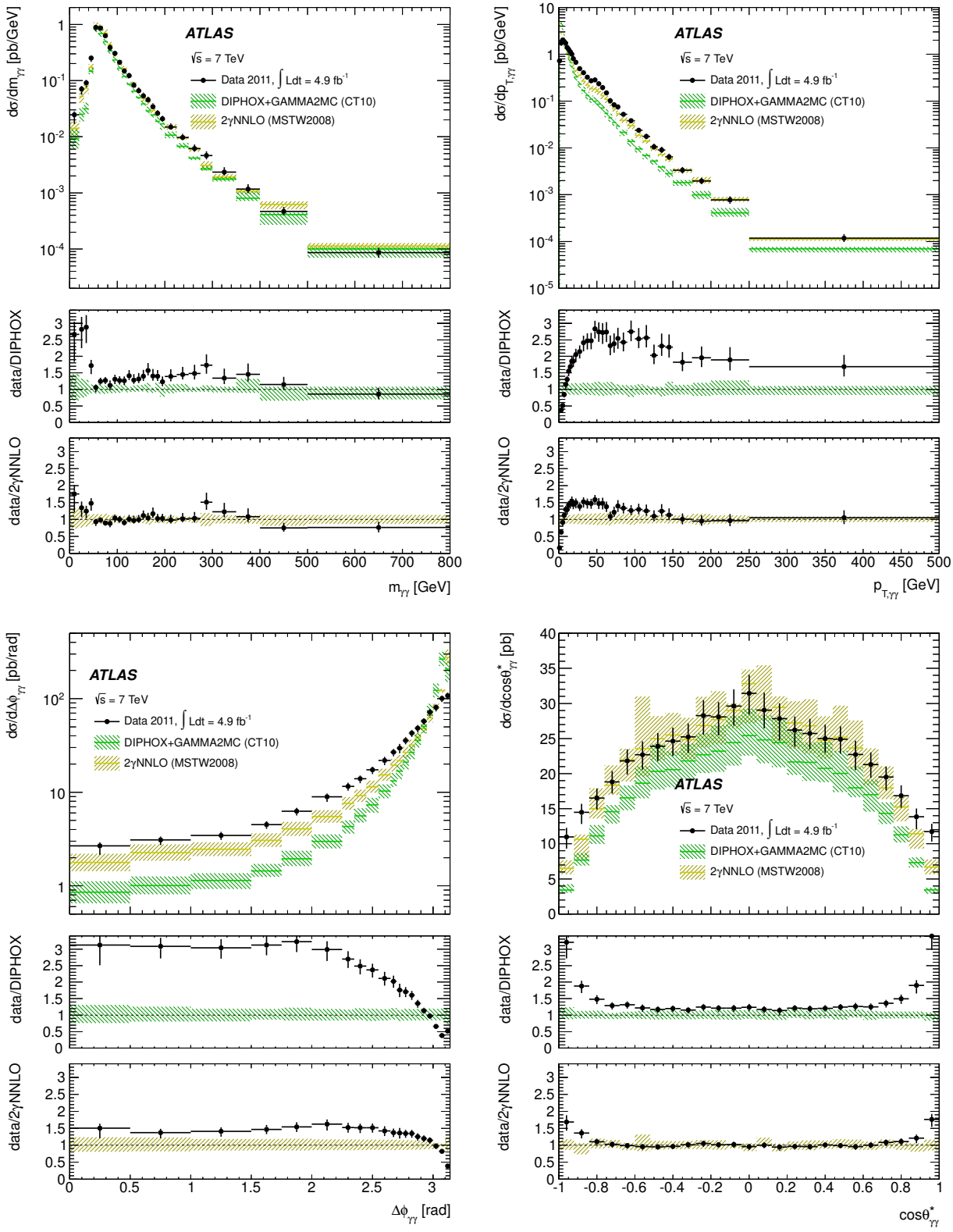

Figure 29: Comparison between the experimental cross sections and the predictions obtained with DIPHOX+GAMMA2MC (NLO) and 2γNNLO (NNLO): $m_{\gamma\gamma}$ (top left), $p_{\mathrm{T},\gamma\gamma}$ (top right), $\Delta\phi_{\gamma\gamma}$ (bottom left), $\cos\theta^*_{\gamma\gamma}$(bottom right). Black dots correspond to data with with error bars for their total uncertainties, which are dominated by the systematic component. The theoretical uncertainties include contributions from the limited size of the simulated sample, from the scale choice and from uncertainties on the parton distribution functions and on the hadronization and underlying event corrections.

6 The $H \to \gamma\gamma$ channel

My previously described activities (calorimeter uniformity, isolation, direct photon pair studies) are part of the necessary steps allowing such a discovery like the Higgs Boson in its diphoton decay one. Beyond these "surroundings" activities, I have been involved in various steps of the $H \to \gamma\gamma$ analysis since 2006: I participated in the sensitivity studies that yielded the ultimate performance book of ATLAS before data taking [35] mostly by designing the analysis framework and doing some statistical studies. During the discovery period, my contribution was mostly through performance studies (background decomposition, isolation). And since the discovery, I got interested in studying the angular distributions of the photons coming from the Higgs Boson, which rapidly turned into a spin analysis: I will shortly describe this analysis below. From April 2014 to April 2015, I co-convened the $H \to \gamma\gamma$ subgroup in ATLAS, and thus supervised most of the run 1 publications coming out from this channel (12 publications during my "mandate"). I will not make a summary of all these results, which are documented in references [36–47].

6.1 Study of the spin of the new boson: introduction

It took less than two years of LHC running to discover a Higgs Boson, but it will take many more years to measure its properties precisely enough to rule out the possibility that this is not the Higgs Boson from the Standard Model. One of the first alternatives that could be ruled out, nevertheless, is that the newly discovered boson is not a scalar. The vector (spin 1) alternative is highly disfavored by the observation of its $\gamma\gamma$ decay, because of the Landau-Yang theorem [9]. Even though higher spin values are very unlikely from theoretical prejudice (in particular because one would expect the phenomenology of a spin 2 particle to be rather different from what was already observed), the tensor alternative was tested by both ATLAS and CMS collaborations.

I participated in the two spin analyses performed with the $H \to \gamma\gamma$ channel: the 2013 Moriond analysis [48], and the final run 1 analysis [38], with an improved theoretical model and experimental analysis, that is described here. For me, the interest of this study does not lie so much in the physics outcome (it is extremely unlikely that the newly observed particle could be of spin 2), but rather in the experimental analysis itself (the study of differential distributions of the Higgs Boson events), and in the use of an effective field theory. I contributed to all steps of the analysis, both on the experimental side (analysis strategy, selection, statistical analysis, systematic uncertainties studies) and on the theory "hypothesis testing" side. I studied extensively the spin 2 predictions and I contributed to introduce to ATLAS the multi-leg predictions from MadGraph5_aMC@NLO [54] , and the non-universal couplings models (described below).

6.2 Theoretical spin 2 model

A fundamental spin 2 particle couples to the energy-momentum tensors of other particles and gives rise to gravitation. It is nevertheless massless because gravitation appears to have an unlimited range [10]. But massive spin 2 particles can arise in extra dimension models: for example, both the popular Arkani-Hamed-Dimopoulos-Dvali (ADD) [51] and Randall-Sundrum [52] models have Kaluza-Klein towers of spin-2 gravitons.

More generically (*i.e.* without entering into the details of specific theories), the description of the interaction of a spin-2 particle with fermions and vector bosons is described by the following

[9] An on-shell spin one particle cannot decay into two massless identical particles

[10] There are tentatives to build massive gravity models (see *e.g.* these reviews: [49, 50]), for example to solve the dark energy problem, but with a graviton mass that is totally outside the scope of what can be probed at the LHC.

Lagrangian [53],:

$$\mathcal{L}_2 = -\frac{1}{\Lambda}\left[\sum_V \kappa_V \mathcal{T}^V_{\mu\nu} X^{\mu\nu} + \sum_f \kappa_f \mathcal{T}^f_{\mu\nu} X^{\mu\nu}\right]. \tag{13}$$

The spin-2 tensor field $X^{\mu\nu}$ interacts with the energy-momentum tensors, $\mathcal{T}^V_{\mu\nu}$ and $\mathcal{T}^f_{\mu\nu}$, of any vector boson V and fermion f, as inspired by gravitation theories. The strength of each interaction is determined by the couplings κ_V and κ_f. In the simplest formulation, all couplings are equal. This scenario is referred to as universal couplings (UC), while scenarios with different values of the couplings are referred to as non-universal couplings (non-UC). In the UC scenario, the production of a spin-2 particle in pp collisions is expected to be dominated by QCD processes, with negligible contributions from electroweak (EW) processes (i.e. from processes involving EW boson propagators). Simulation studies based on MadGraph5_aMC@NLO [54] , which implements the Lagrangian described in Eq. (13), predict for the production cross section in the UC scenario $\sigma_{\mathrm{EW}}/\sigma_{\mathrm{QCD}} \simeq 3 \times 10^{-4}$. These studies also show that EW production of the spin-2 resonance would occur mainly in association with a massive EW boson (WX, ZX). Present observations do not show a dominant VH production mechanism, hence suggesting that σ_{EW} is significantly smaller than σ_{QCD}. This analysis therefore considers only QCD production for all the spin-2 benchmark scenarios.

The UC models predict a branching ratio of about 5% to photon pairs and negligible branching ratios to massive EW gauge boson pairs, WW^* and ZZ^*. This prediction is disfavoured by the experimental measurements [55–57] and therefore the equality between all couplings κ cannot hold. In the benchmark scenarios studied in this analysis, each of the couplings κ_W, κ_Z, and κ_γ is assumed to be independent of all the other couplings. In the following, the UC scenario only refers to $\kappa_q = \kappa_g$, without implying the equality for the other κ values.

The simplest QCD production processes, $gg \to X$ and $q\bar{q} \to X$ (where q refers to light quarks), yield different polarisations for the spin-2 particle X, and hence different angular distributions of its decay products. These mechanisms are considered in the model of a graviton-like tensor with minimal couplings proposed in Refs. [58, 59], which has been studied experimentally in Ref. [48]. The EFT Lagrangian, however, also allows for more complex processes with emission of one or more additional partons. For instance, processes with one-parton emission, like $qg \to qX$ and $\bar{q}g \to \bar{q}X$, can produce a spin-2 state through either a qqX or a ggX vertex. When two partons are emitted, as in $gg \to q\bar{q}X$ or $q\bar{q} \to q\bar{q}X$, the spin-2 production may occur through qqX or ggX vertices, respectively, such that the polarisation of X is not uniquely determined by the initial state. Moreover, the EFT also allows for four-leg vertices like $qqgX$. These additional diagrams effectively change the polarisation of the particle X, compared to what is assumed by the model in Refs. [58, 59]. As a consequence, the angular distributions of the decay products become harder to separate from those expected for a scalar resonance.

The QCD production of a spin-2 particle is driven by the values of the couplings κ_g, κ_q. Presently, there are no experimental constraints on the ratio κ_q/κ_g from observed decay modes, since the separation of jets initiated by gluons or by light quarks is experimentally difficult and has not yet been attempted in Higgs boson studies. The ratio κ_q/κ_g can thus be regarded as a free parameter. When $\kappa_q \neq \kappa_g$, the spin-2 model predicts an enhancement of the tail of the distribution of the transverse momentum, p_{T}^X, of the spin-2 particle. Such a high-p_{T}^X tail is not present for the $\kappa_q = \kappa_g$ (UC) case. As stated before, however, the EFTs are valid only up to some energy scale, Λ. At higher energies, new physics phenomena are expected to enter to regularise the anomalous ultra-violet behaviour.

In the present analysis, a selection $p_{\mathrm{T}}^X < 300$ GeV is applied when investigating non-UC scenarios, $\kappa_q \neq \kappa_g$. In addition, for the non-UC scenarios, analyses using a tighter selection $p_{\mathrm{T}}^X < 125$ GeV are also performed. This is a conservative choice for the p_{T}^X selection, as the EFT must describe the physics at least up to the mass of the observed resonance. It has been verified that the choice of the p_{T}^X

selection does not affect the results for the UC scenario. Even assuming the $p_{\mathrm{T}}^{X} < 300$ GeV selection, some choices of κ_q/κ_g produce high-p_{T}^{X} tails incompatible with the observed differential distribution reported in Refs. [44, 60]. For this reason the investigated range of the κ_q/κ_g ratio is limited to between zero and two. The spin-2 scenarios considered in this study are presented in Table 3. The $\kappa_q = \kappa_g$ model is referred to hereafter as the UC scenario. The $\kappa_q = 0$ case implies a negligible coupling to light quarks, whereas the $\kappa_q = 2\kappa_g$ case is an alternative scenario with an enhanced coupling to quarks.

Values of spin-2 quark and gluon couplings		p_{T}^{X} selections (GeV)	
$\kappa_q = \kappa_g$	Universal couplings	–	–
$\kappa_q = 0$	Low light-quark fraction	< 300	< 125
$\kappa_q = 2\kappa_g$	Low gluon fraction	< 300	< 125

Table 3: Choices of the couplings to quarks κ_q and to gluons κ_g studied for the spin-2 benchmark scenarios. The values of the selection criteria applied to the transverse momentum p_{T}^{X} of the spin-2 resonance are also shown. For the UC scenario no p_{T}^{X} selection is applied.

6.3 Statistical treatment

The analyses rely on discriminant observables chosen to be sensitive to the spin and parity of the signal.

A likelihood function, $\mathcal{L}(\text{data} \mid J^P, \mu, \vec{\theta})$, that depends on the spin-parity assumption of the signal is constructed as a product of probabilities over binned distributions of the discriminant observables in each channel:

$$\mathcal{L}(\text{data} \mid J^P, \mu, \vec{\theta}) = \prod_{j}^{N_{\text{chann.}}} \prod_{i}^{N_{\text{bins}}} P\big(N_{i,j} \mid \mu_j \cdot S_{i,j}^{(J^P)}(\vec{\theta}) + B_{i,j}(\vec{\theta})\big) \cdot \mathcal{A}_j(\vec{\theta}) \,, \tag{14}$$

where μ_j represents the parameter associated with the signal rate normalised to the SM prediction in each channel j.[11] The symbol $\vec{\theta}$ represents all nuisance parameters associated to systematic uncertainties (some of them being constrained by auxiliary measurements $\mathcal{A}_j(\vec{\theta})$.). The likelihood function is a product of Poisson distributions P corresponding to the observation of $N_{i,j}$ events in each bin i of the discriminant observables, given the expectations for the signal, $S_{i,j}^{(J^P)}(\vec{\theta})$, and for the background, $B_{i,j}(\vec{\theta})$.

While the couplings are predicted for the SM Higgs boson, they are not known *a priori* for the alternative hypotheses, defined as J^P_{alt}, as discussed in Section 6.2. In order to be insensitive to assumptions on the couplings of the non-SM resonance (the alternative hypotheses) to SM particles, the numbers of signal events in each channel, for each different LHC centre-of-mass energy and for each tested hypothesis, are treated as independent parameters in the likelihood and fitted to the data when deriving results on the spin and parity hypotheses.

The test statistic $\tilde{q}$ used to distinguish between the two spin hypotheses is based on a ratio of profiled likelihoods [61, 62]:

$$\tilde{q} = \log \frac{\mathcal{L}(J^P_{\text{SM}}, \hat{\hat{\mu}}_{J^P_{\text{SM}}}, \hat{\hat{\theta}}_{J^P_{\text{SM}}})}{\mathcal{L}(J^P_{\text{alt}}, \hat{\hat{\mu}}_{J^P_{\text{alt}}}, \hat{\hat{\theta}}_{J^P_{\text{alt}}})} \,, \tag{15}$$

[11] Here channel can be used to indicate different categories in the same final state when producing results for individual decay channels, or different final states when combining them.

where $\mathcal{L}(J^P, \hat{\hat{\mu}}_{J^P}, \hat{\hat{\theta}}_{J^P})$ is the maximum-likelihood estimator, evaluated under either the SM $J^P_{\mathrm{SM}} = 0^+$ or the alternative J^P_{alt} spin-parity hypothesis. The parameters $\hat{\hat{\mu}}_{J^P}$ and $\hat{\hat{\theta}}_{J^P}$ represent the values of the signal strength and nuisance parameters fitted to the data under each spin and parity hypothesis.

The distributions of the test statistic for both hypotheses are obtained using pseudo-experiments. The generation of the pseudo-experiments uses the numbers of signal and background events in each channel obtained from maximum-likelihood fits to data. In the fits of each pseudo-experiment, these and all other nuisance parameters are profiled, i.e. fitted to the value that maximises the likelihood for each value of the parameter of interest.

The distributions of $\tilde{q}$ are used to determine the corresponding p-values $p(J^P_{\mathrm{SM}}) = p^{\mathrm{SM}}$ and $p(J^P_{\mathrm{alt}}) = p^{\mathrm{alt}}$. For a tested hypothesis J^P_{alt}, the observed (expected) p-values are obtained by integrating the corresponding distributions of the test statistic above the observed value of $\tilde{q}$ (above the median of the J^P_{SM} $\tilde{q}$ distribution). When the measured data are in agreement with the tested hypothesis, the observed value of $\tilde{q}$ is distributed such that all p-values are equally probable.

Very small values of the integral of the distribution of the test statistic for the J^P_{alt} hypothesis, corresponding to large values of $\tilde{q}$, are interpreted as the data being in disagreement with the tested hypothesis in favour of the SM hypothesis.

The exclusion of the alternative J^P_{alt} hypothesis in favour of the SM J^P_{SM} hypothesis is evaluated in terms of the modified confidence level $\mathrm{CL_S}(J^P_{\mathrm{alt}})$, defined as [63]:

$$\mathrm{CL_S}(J^P_{\mathrm{alt}}) = \frac{p(J^P_{\mathrm{alt}})}{1 - p(J^P_{\mathrm{SM}})} \,. \tag{16}$$

6.4 Spin analysis in the $H \to \gamma\gamma$ channel

The selection of $H \to \gamma\gamma$ candidate events is based on the procedure of other recent ATLAS $H \to \gamma\gamma$ analyses (see for example Ref. [57]). Events are selected if they satisfy a diphoton trigger criterion requiring loose photon identification, with transverse momentum p_{T} thresholds of 35 GeV and 25 GeV for the photon with the highest (γ_1) and second-highest (γ_2) p_{T}, respectively. During the offline selection two photons are further required to be in a fiducial pseudorapidity region, defined by $|\eta^\gamma| < 2.37$, where the barrel/end-cap transition region $1.37 < |\eta^\gamma| < 1.56$ is excluded. The transverse momentum of the photons must satisfy $p_{\mathrm{T}}^{\gamma_1} > 0.35 \cdot m_{\gamma\gamma}$ and $p_{\mathrm{T}}^{\gamma_2} > 0.25 \cdot m_{\gamma\gamma}$, and only events with a diphoton invariant mass $m_{\gamma\gamma}$ between 105 GeV and 160 GeV are retained. For the events passing this selection, a further requirement is applied on the diphoton transverse momentum, $p_{\mathrm{T}}^{\gamma\gamma} < 300$ GeV, motivated by the assumed validity limit of the spin-2 EFT model, as explained in Section 6.2. After this selection, 17 220 events are left at a centre-of-mass energy $\sqrt{s} = 7$ TeV and 94 540 events at $\sqrt{s} = 8$ TeV.

Kinematic variables sensitive to the spin of the resonance are the diphoton transverse momentum $p_{\mathrm{T}}^{\gamma\gamma}$ and the production angle of the two photons, measured in the Collins–Soper frame [26]:

$$|\cos\theta^*| = \frac{|\sinh(\Delta\eta^{\gamma\gamma})|}{\sqrt{1 + \left(p_{\mathrm{T}}^{\gamma\gamma}/m_{\gamma\gamma}\right)^2}} \frac{2 p_{\mathrm{T}}^{\gamma_1} p_{\mathrm{T}}^{\gamma_2}}{m_{\gamma\gamma}^2} \,, \tag{17}$$

where $\Delta\eta^{\gamma\gamma}$ is the separation in pseudorapidity of the two photons.

The predicted distributions of these variables, for events passing the selection, are shown in Figure 30, for a SM Higgs boson and for a spin-2 particle with different QCD couplings. For the $\kappa_q \neq \kappa_g$ cases, the enhanced high-$p_{\mathrm{T}}^{\gamma\gamma}$ tail offers the best discrimination, whereas for $\kappa_q = \kappa_g$ the most sensitive variable is $|\cos\theta^*|$.

To exploit the signal distribution in both $p_{\mathrm{T}}^{\gamma\gamma}$ and $|\cos\theta^*|$, the selected events are divided into 11 mutually exclusive categories: 10 categories (labelled from C1 to C10) collect events with $p_{\mathrm{T}}^{\gamma\gamma} <$

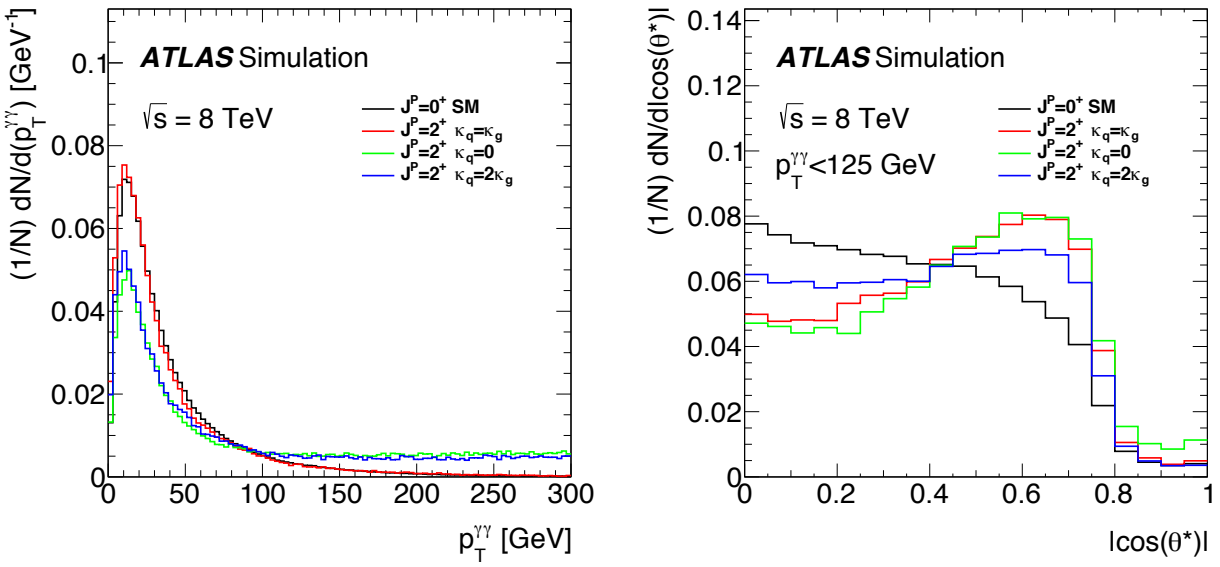

(a) (b)

Figure 30: Expected distributions of kinematic variables sensitive to the spin of the resonance considered in the $H \to \gamma\gamma$ analysis, (a) transverse momentum of the $\gamma\gamma$ system $p_{\mathrm{T}}^{\gamma\gamma}$ and (b) the production angle of the two photons in the Collins-Soper frame $|\cos\theta^*|$, for a SM Higgs boson and for spin-2 particles with three different choices of the QCD couplings.

125 GeV, divided into 10 bins of equal size in $|\cos\theta^*|$, while the 11$^{\mathrm{th}}$ category (labelled C11) groups all events with $p_{\mathrm{T}}^{\gamma\gamma} \geq 125$ GeV. As described in Section 6.2, for the non-UC spin-2 models the analysis is performed with two $p_{\mathrm{T}}^{\gamma\gamma}$ selections, namely $p_{\mathrm{T}}^{\gamma\gamma} < 300$ GeV and $p_{\mathrm{T}}^{\gamma\gamma} < 125$ GeV: the latter case corresponds to not using the 11$^{\mathrm{th}}$ category.

The number of signal events above the continuum background can be estimated through a fit to the observed $m_{\gamma\gamma}$ distribution in each category. The $m_{\gamma\gamma}$ distribution is modelled in each category as the sum of one-dimensional probability density functions (pdf) for signal and background distributions:

$$f^{[c]}(m_{\gamma\gamma}|J) = \frac{n_B^{[c]} f_B^{[c]}(m_{\gamma\gamma}) + (n_J^{[c]} + n_{\mathrm{bias}}^{[c]}) f_S^{[c]}(m_{\gamma\gamma})}{n_B^{[c]} + n_J^{[c]} + n_{\mathrm{bias}}^{[c]}}, \tag{18}$$

where J is the spin hypothesis, $n_B^{[c]}$ and $n_J^{[c]}$ are the background and the signal yield in category c, and $f_B^{[c]}(m_{\gamma\gamma})$, $f_S^{[c]}(m_{\gamma\gamma})$ are the $m_{\gamma\gamma}$ pdfs for the background and the signal, respectively. The signal pdf $f_S^{[c]}(m_{\gamma\gamma})$ is modelled as a weighted sum of a Crystal Ball function, describing the core and the lower mass tail, and of a Gaussian component that improves the description of the tail for higher mass values. For each category, $f_S^{[c]}(m_{\gamma\gamma})$ is fitted to the simulated $m_{\gamma\gamma}$ distribution of the SM Higgs boson and verified to be consistent also with the spin-2 models. The background pdf $f_B^{[c]}(m_{\gamma\gamma})$ is empirically modelled as an exponential of a first- or second-degree polynomial. The choice of such a parameterisation can induce a bias ("spurious signal") in the fitted signal yield, which is accounted for by the term $n_{\mathrm{bias}}^{[c]}$. The size of the expected bias is determined as described in Refs. [44, 57], and ranges between 0.6 and 4 events, depending on the category (with the signal ranging from 15 to more than 100 events). In the statistical analysis, $n_{\mathrm{bias}}^{[c]}$ is constrained for each category by multiplying the likelihood function by a Gaussian function centred at zero and with a width determined by the size

of the expected bias.

Defining n_S as the total signal yield (summed over all categories), the expected fraction of signal events belonging to each category, $\Phi_J^{[c]} \equiv \dfrac{n_J^{[c]}}{n_S}$, depends on the spin hypothesis J. The values of $\Phi_J^{[c]}$ extracted from the data can be compared to their expected values for each spin hypothesis, as shown in Figure 31 for the data collected at $\sqrt{s} = 8$ TeV.

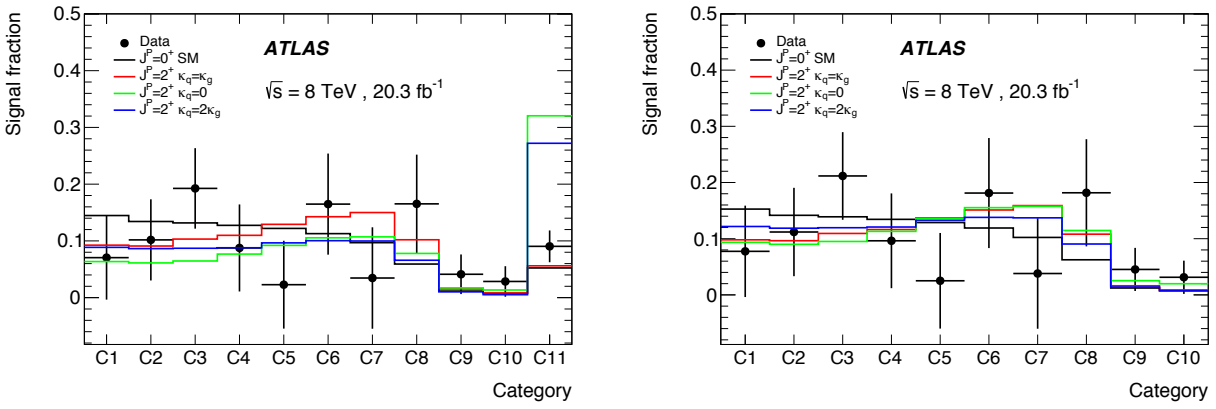

Figure 31: Observed signal fraction per category for the $H \to \gamma\gamma$ analysis, and comparison to expected values for a SM Higgs boson and for a spin-2 particle with different choices of QCD couplings. (a) the 11 categories described in the text are displayed, corresponding to the $p_{\mathrm{T}}^{\gamma\gamma} < 300$ GeV selection; (b) the high-$p_{\mathrm{T}}^{\gamma\gamma}$ category is discarded and the signal fractions are renormalised over the 10 remaining categories, corresponding to the $p_{\mathrm{T}}^{\gamma\gamma} < 125$ GeV selection.

For the non-UC scenario the 11$^{\mathrm{th}}$ (high-$p_{\mathrm{T}}^{\gamma\gamma}$) category provides strong discrimination power against the non-SM hypothesis, as visible in Figure 31(a).

To discriminate between the SM spin-0 ($J^P_{\mathrm{SM}} = 0^+$) and alternative spin-2 hypotheses (J^P_{alt}), two likelihood functions $\mathcal{L}_{J^P_{\mathrm{SM}}}$, $\mathcal{L}_{J^P_{\mathrm{alt}}}$ are built, following the general approach described in Eq. (14):

$$-\ln \mathcal{L}_J = \sum_c \left\{ \left(n_B^{[c]} + n_S \Phi_J^{[c]} + n_{\mathrm{bias}}^{[c]} \right) - \sum_{e \in [c]} \ln \left[n_B^{[c]} f_B^{[c]}(m_{\gamma\gamma}^{(e)}) + (n_S \Phi_J^{[c]} + n_{\mathrm{bias}}^{[c]}) f_S^{[c]}(m_{\gamma\gamma}^{(e)}) \right] \right\} \quad (19)$$

where $\sum_c$ runs over all categories and $\sum_{e \in [c]}$ runs over all events in category c. The total signal yield n_S is a free parameter in the likelihood model. The spin hypothesis being tested enters the likelihood function through the fractions of signal per category, $\Phi_J^{[c]}$.

Several systematic uncertainties enter this model. They are implemented for each spin hypothesis as nuisance parameters, θ_J, constrained by multiplicative Gaussian terms in the likelihood function (not included in Eq. (19) for simplicity).

The signal fractions, $\Phi_J^{[c]}$, for the SM Higgs boson are affected by uncertainties on the p_{T} spectrum of the resonance and on the size of the interference between the resonance and continuum production. The former is computed as described in Ref. [57]. The relative impact on the signal fractions is less than $\pm 1\%$ for categories 1 to 8 ($p_{\mathrm{T}}^{\gamma\gamma} < 125$ GeV and $|\cos\theta^*| < 0.8$), and becomes as large as $\pm 13\%$ for categories 10 and 11. The correction for the interference is evaluated according to Refs. [64, 65]. The systematic uncertainty is conservatively assumed to equal the correction itself, and its relative impact ranges between $\pm 0.1\%$ and $\pm 1.8\%$.

No systematic uncertainty is assigned to the simulated p_{T}^{X} distribution of the spin-2 models. The effect of the interference between the resonance and continuum production is essentially not known, as it depends on the width, Γ_X, of the resonance, which is unknown. The results presented here only hold under the assumption of a narrow width for the resonance, such that interference effects can be neglected.

Additional systematic uncertainties come from the calibration of the photon energy scale and energy resolution and affect the signal parameterisation $f_S^{[c]}$. These uncertainties are evaluated as described in Ref. [66].

6.5 Results

The $H \to \gamma\gamma$ channel is combined with the $H \to ZZ^* \to 4\ell$ and the $H \to WW^* \to e\nu\mu\nu$ channels. The distributions of discriminant variables in data agree with the SM predictions for all three channels, and exclusion ranges for alternative spin hypotheses are derived. Some examples of distributions of the test statistic $\tilde{q}$ (defined in Section 6.3) used to derive the results are presented in Figure 32. In this figure, the observed value is indicated by the vertical solid line and the expected medians by the dashed lines. The shaded areas correspond to the integrals of the expected distributions used to compute the p-values for the rejection of each hypothesis. The signal strengths per decay channel and per centre-of-mass energy are treated as independent parameters in each fit. Their values are compatible with the SM predictions.

The results obtained from the fit to the data, expressed in terms of p-values for different tested hypotheses and observed $\mathrm{CL_S}$ for the alternative hypotheses, are summarised in Tables 4 and 5. The sensitivity to reject alternative hypotheses is driven by the $H \to ZZ^* \to 4\ell$ and the $H \to WW^* \to e\nu\mu\nu$ channels. The $H \to \gamma\gamma$ channel has sizeable sensitivity only to spin-2 models where the $p_{\mathrm{T}}^{X} < 125$ GeV selection is not applied. In all cases the data prefer the SM hypothesis to the alternative models, with the exception of some of the spin-2 models for the $H \to \gamma\gamma$ channel. In this case both hypotheses have similar observed p-values, but neither of the two is below 10% .

As summarised in Table 5, the p-values of the combined results for the three channels show good agreement between the data and the SM hypothesis for all performed tests. All tested alternative hypotheses are rejected at a more than 99.9% confidence level (CL) in favour of the SM hypothesis.

Tested Hypothesis	$H \to \gamma\gamma$				
	$p^{\mathrm{alt}}_{\mathrm{exp},\mu=1}$	$p^{\mathrm{alt}}_{\mathrm{exp},\mu=\hat{\mu}}$	$p^{\mathrm{SM}}_{\mathrm{obs}}$	$p^{\mathrm{alt}}_{\mathrm{obs}}$	Obs. $\mathrm{CL_S}$ (%)
$2^+(\kappa_q = \kappa_g)$	0.13	$7.5 \cdot 10^{-2}$	0.13	0.34	39
$2^+(\kappa_q = 0;\ p_{\mathrm{T}} < 300$ GeV)	$4.3 \cdot 10^{-4}$	$< 3.1 \cdot 10^{-5}$	0.16	$2.9{\cdot}10^{-4}$	$3.5{\cdot}10^{-2}$
$2^+(\kappa_q = 0;\ p_{\mathrm{T}} < 125$ GeV)	$9.4 \cdot 10^{-2}$	$5.6{\cdot}10^{-2}$	0.23	0.20	26
$2^+(\kappa_q = 2\kappa_g;\ p_{\mathrm{T}} < 300$ GeV)	$9.1 \cdot 10^{-4}$	$< 3.1 \cdot 10^{-5}$	0.16	$8.6{\cdot}10^{-4}$	0.10
$2^+(\kappa_q = 2\kappa_g;\ p_{\mathrm{T}} < 125$ GeV)	0.27	0.24	0.20	0.54	68

Table 4: Expected and observed p-values for different spin-parity hypotheses, for each of the channel $H \to \gamma\gamma$. The observed $\mathrm{CL_S}$ for the alternative hypotheses are reported in the last column.

6.6 Conclusion

The combined spin analysis of $H \to \gamma\gamma$, $H \to ZZ^* \to 4\ell$ and $H \to WW^* \to e\nu\mu\nu$ allowed to experimentally rule out that the newly observed particle could be a spin 2 state (though this was already ruled out by "common sense"). Most importantly, this work allowed to enter the era of Higgs

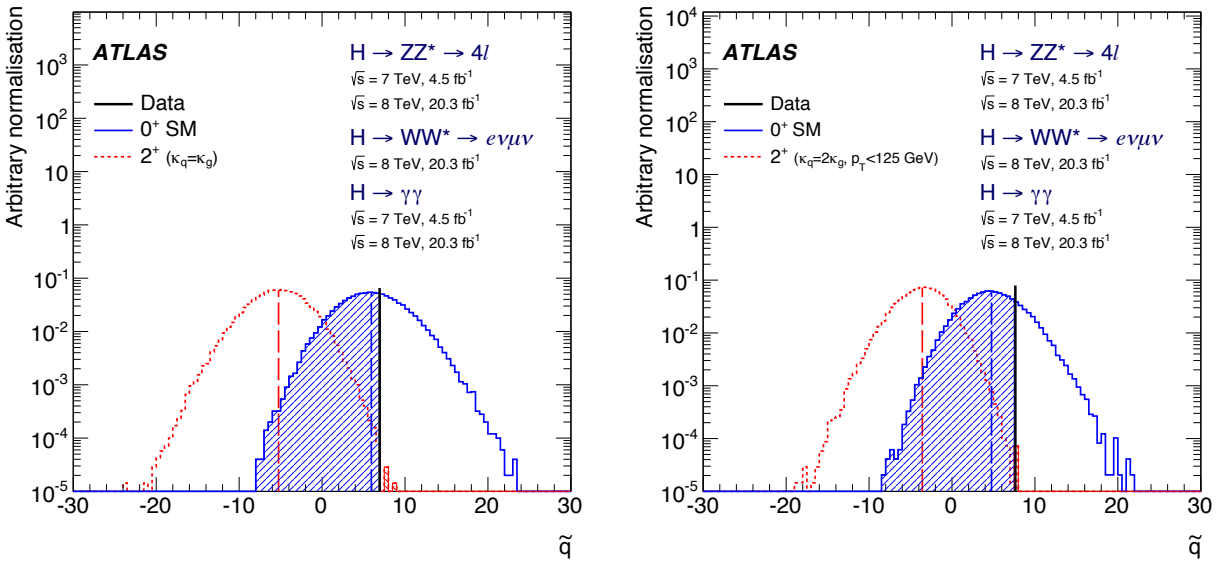

(a) (b)

Figure 32: Examples of distributions of the test statistic $\tilde{q}$, for the combination of decay channels. (a): 0^+ versus the spin-2 model with universal couplings ($\kappa_q = \kappa_g$); (b): 0^+ versus the spin-2 model with $\kappa_q = 2\kappa_g$ and the p_{T} selection at 125 GeV. The observed values are indicated by the vertical solid line and the expected medians by the dashed lines. The shaded areas correspond to the integrals of the expected distributions used to compute the p-values for the rejection of each hypothesis.

Tested Hypothesis	$p^{\text{alt}}_{\text{exp},\mu=1}$	$p^{\text{alt}}_{\text{exp},\mu=\hat{\mu}}$	$p^{\text{SM}}_{\text{obs}}$	$p^{\text{alt}}_{\text{obs}}$	Obs. CL_S (%)
$2^+(\kappa_q = \kappa_g)$	$4.3 \cdot 10^{-3}$	$2.9 \cdot 10^{-4}$	0.61	$4.3 \cdot 10^{-5}$	$1.1 \cdot 10^{-2}$
$2^+(\kappa_q = 0;\ p_\text{T} < 300$ GeV)	$< 3.1 \cdot 10^{-5}$	$< 3.1 \cdot 10^{-5}$	0.52	$< 3.1 \cdot 10^{-5}$	$< 6.5 \cdot 10^{-3}$
$2^+(\kappa_q = 0;\ p_\text{T} < 125$ GeV)	$3.4 \cdot 10^{-3}$	$3.9 \cdot 10^{-4}$	0.71	$4.3 \cdot 10^{-5}$	$1.5 \cdot 10^{-2}$
$2^+(\kappa_q = 2\kappa_g;\ p_\text{T} < 300$ GeV)	$< 3.1 \cdot 10^{-5}$	$< 3.1 \cdot 10^{-5}$	0.28	$< 3.1 \cdot 10^{-5}$	$< 4.3 \cdot 10^{-3}$
$2^+(\kappa_q = 2\kappa_g;\ p_\text{T} < 125$ GeV)	$7.8 \cdot 10^{-3}$	$1.2 \cdot 10^{-3}$	0.80	$7.3 \cdot 10^{-5}$	$3.7 \cdot 10^{-2}$

Table 5: Expected and observed p-values for different spin-parity hypotheses, for the combination of the three channels: $H \to \gamma\gamma$, $H \to ZZ^* \to 4\ell$ and $H \to WW^* \to e\nu\mu\nu$. The observed CL_S for the alternative hypothesis is reported in the last column.

Effective Field Theories, that will be extensively used also in run 2 for further studies of the spin 0 resonance.

7 Conclusions

The LHC run 1 data allowed to finally confirm the existence of the long-awaited Higgs Boson at a mass of around 125 GeV. I feel very lucky to have been able to participate to several steps of this discovery, covering detector and performance studies, analysis tasks, and management of sub-groups. Running the experiment and getting results out of it is not only a scientific challenge, but also a human one: in this respect, the LHC environnement is a very successful and rewarding micro-society in which I enjoyed working a lot.

The LHC run 2 is now starting, upgrading the energy from 8 to 13 TeV, with lots of expectations: we all hope to discover new phenomena during this new run. The run 2 program of the Higgs to two photons channel is very reach: this signature can be used to probe the production of heavier states decaying into the 125 GeV Higgs Boson; the di-higgs production in order to measure the trilinear couplings of the Higgs Boson; or other resonances (other Higgs Bosons, or exotic particles such as gravitons) decaying into two photons. The properties of the 125 GeV Higgs Boson will also be further scrutinized with more precise mass, couplings, CP-related measurements. The phenomenological frameworks to perform these precision measurement are also evolving between run 1 and run 2: beyond simply using the different channel rates to probe the couplings, one can exploit the full differential cross-sections within for example an effective field theory of new physics (since this new physics has not been observed so far, it can indeed be integrated out).

We should also progress on the understanding of the (already impressive) performances of the detectors: for example, improving the Higgs Boson mass measurement in the diphoton decay will require to better understand the electromagnetic calorimeter performances (in particular, the poor description of the lateral shower shape by the simulation). There are also several ideas on how to improve the isolation energy behavior and thus related systematic uncertainties (better core subtraction, refined techniques to get data-driven measurements, ...).

Finally, progresses can also be made on analysis techniques, such as better ways to estimate the systematic uncertainties linked to the analytical fit of the background, or optimize analyses to be at the same time as optimal as possible but also as model-independent as possible.

References

[1] F. Englert and R. Brout, *Broken Symmetry and the Mass of Gauge Vector Mesons*, Phys. Rev. Lett. **13** (1964) pp. 321–323.

[2] P. W. Higgs, *Broken symmetries, massless particles and gauge fields*, Phys. Lett. **12** (1964) pp. 132–133.

[3] P. W. Higgs, *Broken Symmetries and the Masses of Gauge Bosons*, Phys. Rev. Lett. **13** (1964) pp. 508–509.

[4] G. S. Guralnik, C. R. Hagen, and T. W. B. Kibble, *Global Conservation Laws and Massless Particles*, Phys. Rev. Lett. **13** (1964) pp. 585–587.

[5] P. W. Higgs, *Spontaneous Symmetry Breakdown without Massless Bosons*, Phys. Rev. **145** (1966) pp. 1156–1163.

[6] T. W. B. Kibble, *Symmetry breaking in nonAbelian gauge theories*, Phys. Rev. **155** (1967) pp. 1554–1561.

[7] L. Evans and P. Bryant, *LHC Machine*, JINST **3** (2008) S08001.

[8] ATLAS Collaboration, *The ATLAS Experiment at the CERN Large Hadron Collider*, JINST **3** (2008) S08003.

[9] ATLAS Collaboration, *The ATLAS experiment at the CERN Large Hadron Collider*, JINST **3** (2008) S08003.

[10] B. Aubert *et al.*, *Construction, assembly and tests of the ATLAS electromagnetic barrel calorimeter*, NIMA **558** (2006) p. 388.

[11] M. Aleksa*et al.*, *Construction, assembly and tests of the ATLAS electromagnetic end-cap calorimeter*, JINST **3** (2008) P06002.

[12] M.L. Andrieux*et al.*, *Construction and test of the first two sectors of the ATLAS liquid argon presampler*, NIMA **479** (2002) p. 316.

[13] D.M. Gingrich*et al.*, *Construction, assembly and testing of the ATLAS hadronic end-cap calorimeter*, JINST **2** (2007) P05005.

[14] A. Artamonov*et al.*, *The ATLAS forward calorimeters*, JINST **3** (2008) P02010.

[15] M. Aharrouche *et al.*, *Response uniformity of the ATLAS liquid argon electromagnetic calorimeter*, NIMA **582** (2007) p. 429.

[16] ATLAS Collaboration, *Readiness of the ATLAS liquid argon calorimeter for LHC collisions*, Eur. Phys. J. C **70** (2010) pp. 723–753.

[17] M. Cooke *et al.*, "Performance of the ATLAS electromagnetic calorimeter for pizero to two photons and eta to two photons events", ATLAS-CONF-2010-006, 2010.

[18] M. Aurousseau, "Mesure in situ de l'uniformité du calorimètre électromagnétique et recherche des premiers évenements di-photons dans ATLAS", PhD thesis: Université de Savoie, 2011.

[19] S. Paganis,
ATLAS Liquid Argon Barrel Calorimeter Performance in the 2004 CombinedTest-Beam,
Nucl.Phys.Proc.Suppl **172** (2007) p. 108.

[20] ATLAS Collaboration,
Electron and photon energy calibration with the ATLAS detector using LHC Run 1 data,
Eur. Phys. J. C **74** (2014) p. 3071, arXiv: 1407.5063 [hep-ex].

[21] ATLAS Collaboration, *Calorimeter Clustering Algorithms: Description and Performance*,
ATL-LARG-PUB-2008-002, 2008, URL: http://cds.cern.ch/record/1099735.

[22] M. Cacciari, G. P. Salam, and G. Soyez, *FastJet user manual*,
Eur. Phys. J. **C 72** (2012) p. 1896.

[23] ATLAS Collaboration, *Electron efficiency measurements with the ATLAS detector using the 2012 LHC proton–proton collision data*, ATLAS-CONF-2014-032, 2014,
URL: http://cdsweb.cern.ch/record/1706245.

[24] ATLAS Collaboration, *Measurement of the isolated diphoton cross section in pp collisions at* $\sqrt{s} = 7$ *TeV with the ATLAS detector*, Phys. Rev. D **85** (2012) p. 012003,
arXiv: 1107.0581 [hep-ex].

[25] ATLAS Collaboration, *Measurement of isolated-photon pair production in pp collisions at* $\sqrt{s} = 7$ *TeV with the ATLAS detector*, JHEP **1301** (2013) p. 086, arXiv: 1211.1913 [hep-ex].

[26] J. C. Collins and D. E. Soper,
Angular distribution of dileptons in high-energy hadron collisions,
Phys. Rev. D **16** (1977) p. 2219.

[27] T. Sjöstrand, S. Mrenna, and P. Z. Skands, *PYTHIA 6.4 physics and manual*,
JHEP **0605** (2006) p. 026.

[28] T Gleisberg et al., *SHERPA 1.alpha, a proof-of-concept version*,
J. High Energy Phys. **02** (2003) 056. 28 p, arXiv: hep-ph/0311263.

[29] T. Binoth et al., *Hard photon production and matrix-element parton-shower merging*,
Eur. Phys. J. **C 16** (2000) p. 311.

[30] Z. Bern, L. Dixon, and C. Schmidt,
Isolating a light Higgs boson from the diphoton background at the LHC,
Phys. Rev. D **66** (2002) p. 074018.

[31] S. Catani, L. Cieri, D. de Florian, G. Ferrera, and M. Grazzini,
Diphoton production at hadron colliders: a fully-differential QCD calculation at NNLO,
Phys. Rev. Lett. **108** (2012) p. 072001.

[32] ATLAS Collaboration, *Measurement of the inclusive isolated prompt photon cross section in pp collisions at* $\sqrt{s} = 7$ *TeV with the ATLAS detector*, Phys. Rev. D **83** (2011) p. 052005,
arXiv: 1012.4389 [hep-ex].

[33] ATLAS Collaboration, *Electron performance measurements with the ATLAS detector using the 2010 LHC proton–proton collision data*, Eur. Phys. J. C **72** (2012) p. 1909,
arXiv: 1110.3174 [hep-ex].

[34] ATLAS Collaboration, *Measurements of the photon identification efficiency with the ATLAS detector using* 4.9 fb^{-1} *of pp collision data collected in 2011*, ATLAS-CONF-2012-123, 2012,
URL: http://cdsweb.cern.ch/record/1473426.

[35] G. Aad et al.,
Expected Performance of the ATLAS Experiment - Detector, Trigger and Physics (2009), arXiv: 0901.0512 [hep-ex].

[36] G. Aad et al., *Combined Measurement of the Higgs Boson Mass in pp Collisions at $\sqrt{s} = 7$ and 8 TeV with the ATLAS and CMS Experiments*, Phys. Rev. Lett. **114** (2015) p. 191803, arXiv: 1503.07589 [hep-ex].

[37] G. Aad et al.,
Measurements of the Total and Differential Higgs Boson Production Cross Sections Combining the H??? and H?ZZ?4? Decay Channels at $\sqrt{s}$=8??TeV with the ATLAS Detector*, Phys. Rev. Lett. **115**.9 (2015) p. 091801, arXiv: 1504.05833 [hep-ex].

[38] G. Aad et al.,
Study of the spin and parity of the Higgs boson in diboson decays with the ATLAS detector, Eur. Phys. J. **C75**.10 (2015) p. 476, arXiv: 1506.05669 [hep-ex].

[39] G. Aad et al., *Measurements of the Higgs boson production and decay rates and coupling strengths using pp collision data at $\sqrt{s} = 7$ and 8 TeV in the ATLAS experiment* (2015), arXiv: 1507.04548 [hep-ex].

[40] G. Aad et al., *Searches for Higgs boson pair production in the $hh \to bb\tau\tau, \gamma\gamma WW*, \gamma\gamma bb, bbbb$ channels with the ATLAS detector* (2015), arXiv: 1509.04670 [hep-ex].

[41] G. Aad et al., *Constraints on non-Standard Model Higgs boson interactions in an effective field theory using differential cross sections measured in the $H \to \gamma\gamma$ decay channel at $\sqrt{s} = 8$ TeV with the ATLAS detector* (2015), arXiv: 1508.02507 [hep-ex].

[42] G. Aad et al.,
Search for Dark Matter in Events with Missing Transverse Momentum and a Higgs Boson Decaying to Two Photons in pp Collisions at $\sqrt{s} = 8$ TeV with the ATLAS Detector, Phys. Rev. Lett. **115**.13 (2015) p. 131801, arXiv: 1506.01081 [hep-ex].

[43] ATLAS Collaboration, *Measurement of Higgs boson production in the diphoton decay channel in pp collisions at center-of-mass energies of 7 and 8 TeV with the ATLAS detector*, Phys. Rev. D **90** (2014) p. 112015, arXiv: 1408.7084 [hep-ex].

[44] ATLAS Collaboration, *Measurements of fiducial and differential cross sections for Higgs boson production in the diphoton decay channel at $\sqrt{s} = 8$ TeV with ATLAS*, JHEP **1409** (2014) p. 112, arXiv: 1407.4222 [hep-ex].

[45] G. Aad et al., *Search for Scalar Diphoton Resonances in the Mass Range $65 - 600$ GeV with the ATLAS Detector in pp Collision Data at $\sqrt{s} = 8$ TeV*, Phys. Rev. Lett. **113**.17 (2014) p. 171801, arXiv: 1407.6583 [hep-ex].

[46] G. Aad et al., *Search For Higgs Boson Pair Production in the $\gamma\gamma b\bar{b}$ Final State using pp Collision Data at $\sqrt{s} = 8$ TeV from the ATLAS Detector*, Phys. Rev. Lett. **114**.8 (2015) p. 081802, arXiv: 1406.5053 [hep-ex].

[47] G. Aad et al., *Measurement of the Higgs boson mass from the $H \to \gamma\gamma$ and $H \to ZZ^* \to 4\ell$ channels with the ATLAS detector using 25 fb^{-1} of pp collision data*, Phys. Rev. **D90**.5 (2014) p. 052004, arXiv: 1406.3827 [hep-ex].

[48] ATLAS Collaboration, *Evidence for the spin-0 nature of the Higgs boson using ATLAS data*, Phys. Lett. B **726** (2013) pp. 120–144, arXiv: 1307.1432 [hep-ex].

[49] C. de Rham, *Massive Gravity*, Living Rev. Rel. **17** (2014) p. 7, arXiv: 1401.4173 [hep-th].

[50] K. Hinterbichler, *Theoretical Aspects of Massive Gravity*, Rev. Mod. Phys. **84** (2012) pp. 671–710, arXiv: 1105.3735 [hep-th].

[51] N. Arkani-Hamed, S. Dimopoulos, and G. R. Dvali, *The Hierarchy problem and new dimensions at a millimeter*, Phys. Lett. **B429** (1998) pp. 263–272, arXiv: hep-ph/9803315 [hep-ph].

[52] L. Randall and R. Sundrum, *A Large mass hierarchy from a small extra dimension*, Phys. Rev. Lett. **83** (1999) pp. 3370–3373, arXiv: hep-ph/9905221 [hep-ph].

[53] P. Artoisenet et al., *A framework for Higgs characterisation*, JHEP **1311** (2013) p. 043, arXiv: 1306.6464 [hep-ph].

[54] J. Alwall et al., *The automated computation of tree-level and next-to-leading order differential cross sections, and their matching to parton shower simulations*, JHEP **1407** (2014) p. 079, arXiv: 1405.0301 [hep-ph].

[55] ATLAS Collaboration, *Measurements of Higgs boson production and couplings in the four-lepton channel in pp collisions at center-of-mass energies of 7 and 8 TeV with the ATLAS detector*, Phys. Rev. D **91** (2015) p. 012006, arXiv: 1408.5191 [hep-ex].

[56] ATLAS Collaboration, *Observation and measurement of Higgs boson decays to WW^* with the ATLAS detector*, Submitted to Phys. Rev. D (2014), arXiv: 1412.2641 [hep-ex].

[57] ATLAS Collaboration, *Measurement of Higgs boson production in the diphoton decay channel in pp collisions at center-of-mass energies of 7 and 8 TeV with the ATLAS detector*, Phys. Rev. D **90** (2014) p. 112015, arXiv: 1408.7084 [hep-ex].

[58] Y. Gao et al., *Spin determination of single-produced resonances at hadron colliders*, Phys. Rev. D **81** (2010) p. 075022, arXiv: 1001.3396 [hep-ph].

[59] S. Bolognesi et al., *On the spin and parity of a single-produced resonance at the LHC*, Phys. Rev. D **86** (2012) p. 095031, arXiv: 1208.4018 [hep-ph].

[60] ATLAS Collaboration, *Fiducial and differential cross sections of Higgs boson production measured in the four-lepton decay channel in pp collisions at $\sqrt{s}$=8 TeV with the ATLAS detector*, Phys. Lett. B **738** (2014) pp. 234–253, arXiv: 1408.3226 [hep-ex].

[61] G. Cowan et al., *Asymptotic formulae for likelihood-based tests of new physics*, Eur. Phys. J. C **71** (2011) p. 1554, arXiv: 1007.1727v2 [physics.data-an].

[62] G. Cowan et al., *Erratum to: Asymptotic formulae for likelihood-based tests of new physics*, Eur. Phys. J. C **73**.7, 2501 (2013).

[63] A. L. Read, *Presentation of search results: The CL_s technique*, J. Phys. G **28** (2002) p. 2693.

[64] L. Dixon and M. Siu, *Resonance continuum interference in the diphoton Higgs signal at the LHC*, Phys. Rev. Lett. B **90** (2003) p. 252001, arxiv: hep-ph/0302233.

[65] L. Dixon and Y. Li, *Bounding the Higgs Boson Width Through Interferometry*, Phys. Rev. Lett. B **111** (2013) p. 111802, arxiv: hep-ph/1305.3854.

[66] ATLAS Collaboration, *Measurement of the Higgs boson mass from the $H \to \gamma\gamma$ and $H \to ZZ^* \to 4\ell$ channels with the ATLAS detector using 25 fb^{-1} of pp collision data*, Phys. Rev. D **90** (2014) p. 052004, arXiv: 1406.3827 [hep-ex].